UNIVERSIDADE DE LISBOA
FACULDADE DE CIÊNCIAS
DEPARTAMENTO DE FÍSICA

Design and benchmark of an innovative concept to measure light charged particles in the R3B/FAIR experiment using RPCs

Diogo André Afonso Miguel

Mestrado em Engenharia Física

Dissertação orientada por:
Professor Doutor Daniel Galaviz Redondo

2024

Acknowledgements

I would like to begin by expressing my deepest gratitude to my supervisor, Professor Dr. Daniel Galaviz, for his guidance, insightful feedback, and constant support that has been crucial throughout the entirety of this project. His dedication and the time he invested in my work have deeply shaped the trajectory of this thesis and my academic growth, for which I am truly grateful.

I am also deeply appreciative of the financial support provided by LIP for travels and participation in collaboration meetings. Additionally, I would like to thank Eurolabs for financially supporting my stay at GSI. An experience that provided me with a broader perspective and deeper understanding of my field.

My thanks to the NUC-RIA group, where I had the privilege of conducting my research. The collaborative spirit and the intellectual environment within the group were integral to my work. I would like to extend a special thanks to Manuel Xarepe and Tomás Sousa, who were among the first in our group to work at R3B. Their efforts, knowledge, and above all, their friendship, were instrumental in navigating the complexities of this project.

I would also like to express my gratitude to my family. My parents, Rute and Aristides, my grandparents, Glória, Henriqueta, José Afonso, and José Miguel and uncles, Mónica, César and Luís. Your unconditional love, patience, and belief in me have been very important to me and helped in the conclusion of these work. Thank you all for your support and for always being there.

Lastly, I would like to thank my friends, Beatriz, Carolina Felgueiras, Carolina Ribeiro, Eva, Henrique, Lukas, and Olavo. Thank you for always being there, making me laugh, for the late-night conversations, and the much-needed distractions.

Resumo

Este trabalho focou-se no comportamento de um detetor de Câmara de Placas Resistivas (RPC, do inglês *Resistive Plate Chamber*) em combinação com o calorímetro eletromagnético CALIFA para a experiência Reações com Feixes Radioativos Relativisticos (R^3B, do inglês *Reactions with Relativistic Radioactive Beams*), localizada no FAIR, utilizando o R3BRoot como ferramenta de simulação e análise. R3BRoot é uma ferramenta essencial no FAIR que permite modelar e manipular simulações complexas. A análise deste trabalho está repartida em três partes: a primeira é focada na integração do calorímetro CALIFA na simulação e o seu efeito; a segunda parte adiciona um bloco de silício à RPC para melhor simular condições reais, onde existem dispositivos e cabos eletrónicos no caminho das partículas, que afetam as suas características, dispositivos estes essenciais ao funcionamento dos detetores; por último, a análise das resoluções da RPC, onde foi estudado a influência de diferentes resoluções para tempo e posição na reconstrução do momento. No fim juntou-se a influência do bloco de silício e o efeito das resoluções da RPC. Adicionalmente, foi feito um estudo para o conceito do Espetrómetro da linha de protões (PAS, do inglês *Proton-Arm Spectrometer*), utilizando RPCs como alternativa ao sistema pretendido inicialmente.

As RPCs são um tipo de detetor gasoso utilizado em física de partículas e de altas energias para detetar a passagem de partículas carregadas. O seu funcionamento baseia-se no processo de ionização de gases onde, ao atravessar o gás, uma partícula carregada ioniza partes deste. O campo elétrico criado por duas placas resistivas paralelas cria uma avalanche de ionização, gerando um sinal elétrico que é captado por elétrodos posicionados nas placas. Devido à sua alta resistividade, a corrente resultante é mantida localmente permitindo uma ótima resolução na deteção da posição e do tempo de passagem da partícula tornando-as ideais para experiências que exigem medições rápidas e precisas.

A integração do calorímetro CALIFA (CALorimeter for In-Flight detection of gamma-rays and high-energy charged pArticles) em conjunto com a RPC foi um dos primeiros objetivos deste trabalho. O CALIFA é essencial na experiência R^3B, projetado para medir com precisão fotões de alta energia e partículas carregadas leves. Encontra-se posicionado antes do dipolo magnético GLAD e a envolver o local onde se coloca o alvo da experiência. Este calorímetro é composto por 2560 cristais de CsI(Tl), divididos em duas secções: o Barrel, cobrindo ângulos polares de 43º a 140º, e o Forward Endcap, de 7º a 43º. A escolha destes cristais deve-se à sua elevada densidade e eficiência de deteção, que são fundamentais para a absorção completa da energia das partículas. No entanto, existem partículas que são suficientemente energéticas e atravessam completamente os cristais do CALIFA, não sendo devidamente detetadas. Aqui entra a aplicação da RPC explorada neste trabalho. Ao colocar uma RPC por trás do CALIFA, é possível reconstruir o momento das partículas que o atravessam, utilizando a informação do

seu tempo de voo medido na RPC. Este momento tem um desvio em relação ao momento original da partícula devido à presença do CALIFA.

Na segunda parte introduziu-se um bloco de silício no modelo experimental, essencial para perceber de que forma a eletrónica associada ao CALIFA afeta a reconstrução do momento. Este bloco de silício foi utilizado para replicar as interações que as partículas carregadas teriam com materiais reais antes de alcançarem a RPC e o impacto destas nas partículas que o atravessam. A escolha do silício como material deve-se à sua densidade, semelhante à densidade média destes materiais eletrónicos. As simulações indicaram que a introdução do bloco de silício ajudou a replicar os efeitos de dispersão e perda de energia que seriam encontrados em condições reais, proporcionando uma base sólida para esta aplicação. Estas simulações mostraram que este bloco também introduz um desvio no momento reconstruido, mas é menos relevante que o desvio provocado pelo CALIFA. A resolução obtida foi semelhante à resolução do momento quando o bloco não está presente.

A terceira e última parte concentrou-se na análise das resoluções temporais e de posição da RPC, que até então estavam a ser consideradas como ideais. Para fazer este estudo foi acrescentado pequenas variações temporais e espaciais nos valores obtidos. Realizou-se também um estudo mais detalhado para protões de 500 MeV/u utilizando uma matriz de resoluções e que permitiu avaliar as melhores combinações de resoluções de tempo e posição.

A análise deste mapa indicou que a resolução de tempo desempenha um papel mais importante na determinação do momento das partículas, do que a resolução de posição, contudo é desafiante construir uma RPC em que a sua resolução temporal seja abaixo dos 50 picosegundos. Já a resolução espacial apresenta uma menor variação nos valores de resolução de momento e apenas valores de resolução espacial acima dos 3 cm resultam em valores de momento não tão desejados. Para quase todos os valores de resoluções estudados (resolução temporal entre 0 ps e 250 ps e espacial entre 0 cm e os 5 cm), a resolução em momento manteve-se abaixo dos 10% para as partículas estudadas.

Para as energias e partículas restantes estudadas, a análise foi menos abrangente, mas os resultados obtidos reforçam a observação de que a resolução do tempo tem um impacto mais significativo na resolução do momento do que a de posição. Por exemplo, as partículas alfa, sendo cerca de quatro vezes mais massivas que os protões, exibiram um comportamento semelhante, apenas com um desvio em valor absoluto cerca de 0.5 a 1 pontos percentuais acima. O equilíbrio entre a resolução temporal e a resolução espacial é essencial para otimizar o desempenho do detetor, garantindo ao mesmo tempo que o sistema seja viável do ponto de vista prático e económico.

Além deste estudo principal, foi também explorada a utilização de RPCs para o conceito do Proton-Arm Spectrometer (PAS), um dos três braços principais da experiência do R^3B, formando uma parte essencial da configuração experimental. O PAS é uma parte crítica para a deteção de protões e outras partículas carregadas leves com alta precisão posicionado após o GLAD. Originalmente, o PAS foi projetado para utilizar paredes de tubo de palha (do inglês Straw-Tube Walls (STW)), como uma contribuição da Rússia. Estes detetores estavam projetados para alcançar uma resolução de momento da ordem de 10^{-3}, com uma resolução angular inferior a $1\,\mathrm{mrad}$ e uma precisão de posição abaixo dos $150\,\mu\mathrm{m}$. Estas especificações são vitais para garantir que o sistema possa detetar com precisão as trajetórias das partículas em ambientes de alta energia, como aqueles encontrados no R^3B. Contudo a contribuição russa deixou

de ser viável, e portanto foi necessário arranjar uma solução alternativa. Para isso foi estudada a possibilidade de usar RPCs como conceito de deteção alternativo.

A exploração de alternativas aos STWs levou à avaliação de três configurações utilizando fibras e RPCs: um setup apenas com fibras, uma combinação de fibras com RPCs e um setup apenas com duas RPCs. Neste trabalho são apresentados os resultados referentes à configuração com as duas RPCs com o principal foco na resolução em momento alcançada. As simulações foram feitas em ambientes de vácuo, hélio e ar e revelaram que o método de ajuste Multi-Dimensional (MDF) dependente do Tempo de Voo (ToF) ofereceu melhores resoluções de momento do que o método dependente da posição. No entanto, nenhum dos métodos alcançou o objetivo de resolução em momento de 0,1% para o PAS, com os melhores resultados do MDF dependente do ToF a atingirem 0,68%. O meio em que se realizou as simulações teve um papel significativo no método dependente da posição, sendon o ar o meio com o pior desempenho, enquanto o método dependente do ToF manteve-se robusto em diferentes ambientes. O design baseado em RPCs não foi selecionado para o PAS, optando-se antes por um setup de três planos de fibras, que demonstrou um desempenho superior, alinhando-se com os resultados originais dos tubos de palha.

Em conclusão, o trabalho desenvolvido nesta dissertação ajudou a promover o desenvolvimento de tecnologias de deteção de partículas em física de altas energias, ao usar RPCs na experiência R^3B.

Palavras Chave: Resolução de momento, RPC, CALIFA, R3B/FAIR, Física de altas energias

Abstract

This work focused on analyzing the behavior of a Resistive Plate Chamber (RPC) detector for the Reactions with Relativistic Radioactive Beams (R^3B) experiment at the Facility for Antiprotons and Ion Research (FAIR), utilizing the R3BRoot simulation framework. The study was divided into three main parts.

Firstly, the CALIFA calorimeter was integrated into the simulations to assess its impact on the reconstructed values of momentum in the RPC. Secondly, a silicon block was added to the RPC setup to better simulate real-world conditions where electronic components and cables influence particle trajectories and characteristics. Lastly, the study examined the RPC's time and position resolution limitations and their effects on momentum reconstruction accuracy. After this three steps, they were all combined and analyzed. These simulations revealed that CALIFA and the silicon block affected mainly the nominal value of the reconstructed momentum, adding an expected offset that can be corrected. As for the resolutions of the RPC, it worsens the momenta resolution. Time resolution plays a more critical role than spatial resolution in accurate momentum determination, with most configurations achieving momentum resolutions below 10% for the particles studied.

Additionally, the research explored the concept of the Proton-Arm Spectrometer (PAS) by evaluating RPCs as an alternative to the originally proposed straw-tube detectors. The setup studied consisted of two RPCs. Results indicated that while RPC-based designs provided reasonable performance, they did not meet the momentum resolution requirements of PAS, leading to the selection of a configuration utilizing three fiber planes instead.

The findings of this work contribute valuable insights into optimizing detector designs for high-energy physics experiments, ensuring precise and reliable measurements. This research supports ongoing advancements in particle detection technologies, enhancing the capabilities and accuracy of experiments conducted within the R3B.

Keywords: Momentum Resolution, RPC, CALIFA, R3B/FAIR, High Energy Physics

Contents

List of Figures

List of Tables

List of symbols

A - Atomic Number

Q - Charge of a particle

E - Energy

e - Elementary charge

p_0 - Nominal Momentum

σ^2 - Variance

(x, y, z) - Spatial coordinates

E_γ - Photon Energy

N_A - Avogadro's constant

I - Mean excitation energy of the target atom

ρ - Density of the material

E_{max} - Maximum energy transferred in a single collision

γ - Lorentz factor

δ - Density correction term

T - Kinetic energy of the scattered electron

B_e - Binding energy

ω - Probability of Compton interaction per unit distance

S - Stopping power

r_e - Radius of the electron

ΔL^{LS} - Lindhard-Sørenson correction

$\Delta L^{B}(a)$ - Bloch correction

S_0 - Shell correction

β - Ratio between particle velocity and photon velocity in vacuum

N - Number of atoms per unit volume

Z - Atomic number of the target material

z - Atomic number of the beam particles

$\sigma(m^{-1})$ - Probability for Compton interaction to occur per unit distance

T_e - Kinetic energy of the electron

T_{e^+} - Kinetic energy of the positron

m - Mass

m_p - Proton mass

m_e - Electron mass

m_μ - Muon mass

c - Speed of light in vacuum

P - Momentum

ΔX, ΔY - Spatial resolutions in the x and y axes

Δt - Time resolution

σ_θ - Angular resolution

Acronyms

ALICE A Large Ion Collider Experiment. 20

APDs Avalanche Photodiodes. 3

CALIFA CALorimeter for In-Flight detection of gamma-rays and high-energy charged pArticles. 3, 5–7, 27, 41, 55, III

CEPA CALIFA Endcap Phoswich Array. 6

CERN European Council for Nuclear Research. 19

FAIR Facility for Antiprotons and Ion Research. 1, 6, 25, III, VII

FEE Front End Electronics. 24

FRS FRagment Separator. 1

GLAD Large-acceptance dipole magnet. 1, 3, 6, 28, 49, III

LHC Large Hadron Collider. 17

MDF Multi-Dimensional Fit. 49

MIP Minimum Ionizing Particle. 53

MRPC Multigap Resistive Plate Chamber. 21

MWPCs Multi Wire Proportional Chamber. 1

NeuLAND New Large-Area Neutron Detector. 2

PAS Proton-Arm Spectrometer. 7, 49, 52, III

PDs Photodiodes. 3

PMT Photomultiplier Tube. 3

PNPI Petersburg Nuclear Physics Institute. 7

PPAC Parallel-Plate Avalanche Chambers. 20

RIB Rare Isotope Beam. 1

RICH Ring-Imaging Čerenkov Detector. 17

ROLU From the german: right, above, left, below. 1

RPC Resistive Plate Chamber. 2, 6, 7, 20, 22, 23, 52, 55, III, VII

R^{3}B Reactions with Relativistic Radioactive Beams. 1, 3, 4, 6, 7, 19, 24, 25, 27, 39, 41, 49, 50, 52, 55, 56, III–V, VII, XIII

STW Straw-Tube Walls. 7, IV, V

SiPMs Silicon Photomultipliers. 3

Super-FRS Super FRagment Separator. 1

TDR Technical Design Report. 56

TOFD Time Of Flight Detector. 2

ToF Time of Flight. 50

iPhos intrinsic Phoswich. 6

Chapter 1

Introduction

1.1 Motivation

Measuring light-charged particles and their interactions with matter is necessary to understand the fundamental processes that occur on the atomic and sub-atomic levels. Reaching the relativistic regime, these reaction studies fall in the scope of the Reactions with Relativistic Radioactive Beams (R^3B) experiment, of the Facility for Antiprotons and Ion Research (FAIR) in Darmstadt, Germany. Its experimental setup aims at performing complete measurements of all products emerging from induced nuclear reactions, with various detector systems located before the reaction point, around the reaction target, and after a large acceptance dipole magnet that selects the reaction products according to their magnetic rigidity [1].

The R^3B setup, Figure 1.1, covers experimental reaction studies with exotic nuclei far off stability, enabling a diverse physics program with rare-isotope beams, from the analysis of knockout reactions, quasi-free scattering, elastic proton scattering, fission, spallation reactions, astrophysics, among others [2], probing the fundamental properties of these exotic nuclei like their shapes, spins and decay modes. From the production of these exotic nuclei and the experimental tools needed to analyze their properties arise unique experimental challenges. A general constraint is that such nuclei are typically produced with low intensities, demanding highly efficient detection systems with excellent resolving power. Furthermore, the extraction of information on exotic nuclei is facilitated using reactions in which one of the participants has a relatively simple structure like Hydrogen, Deuteron, Helium-3, and Helium-4, creating the need for inverse kinematics. These are reactions where the beam is composed of heavier particles than the particles of the target. At R^3B, a commonly used target is liquid hydrogen [3], for its simple structure and manufacture, low evaporation rate (making it more economical) while also minimizing background noise by reducing multiple scattering contributions within nuclei [4].

Several systems are being developed to study and operate such an enormous physics program. In the R^3B experimental setup, a Rare Isotope Beam (RIB) is injected from the FRagment Separator (FRS) [5], the current fragment separator in use (will change to the Super-FRS[6] in the future). Then, the beam passes through several initial detector systems, such as LOS [7], ROLU, and the MWPCs, after which reaches the target. Inducing the magnetic field that separates the incoming particles from the reaction is GLAD, a large acceptance dipole magnet with a high field integral of $4.8\,\mathrm{Tm}$ [8], establishing the three main branches of study: the Neutron arm, the Heavy Fragment arm, and the Proton arm.

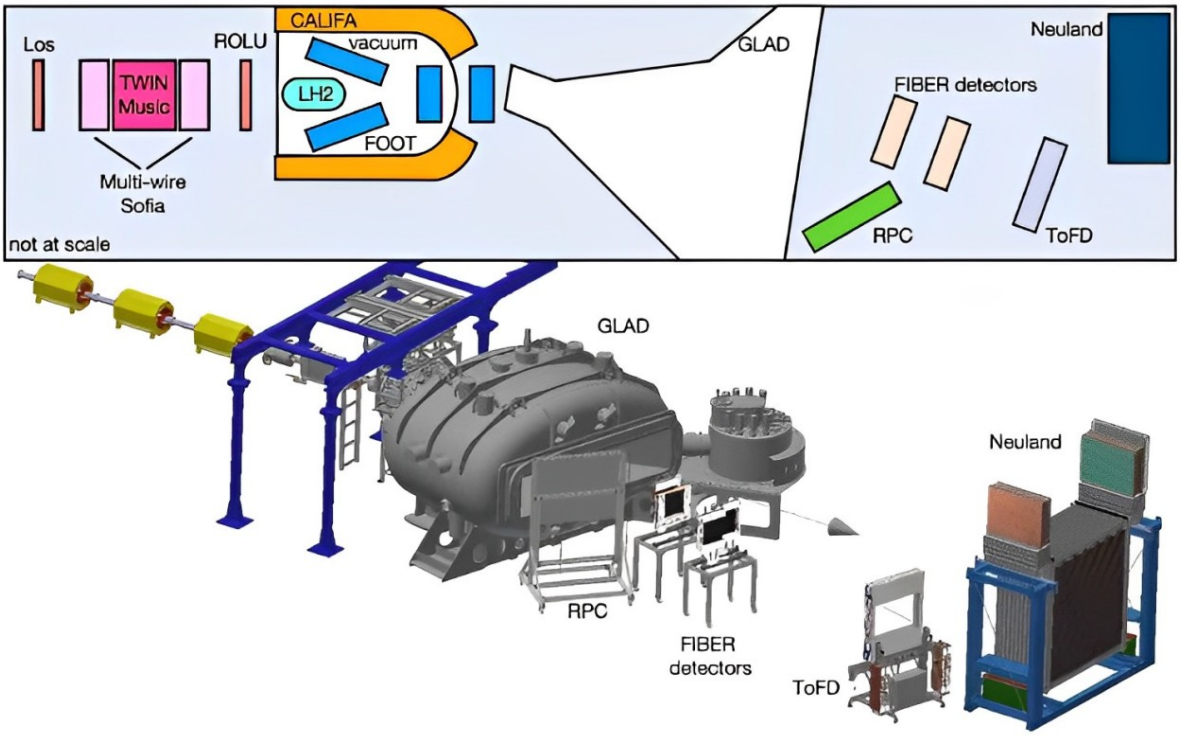

Figure 1.1: R^3B experimental setup. The RIB (Rare Isotope Beam) comes from FRS and hits the target. Surrounding the target is CALIFA and after it is GLAD, which creates the three main branches of study: the Neutron arm, the Heavy Fragment arm, and the Proton arm [9].

The New Large-Area Neutron Detector (NeuLAND), is the detector responsible for the detection of the neutrons in the neutron arm, featuring a high detection efficiency, high resolution, and a large multi-neutron resolving power. It can give a time resolution better than $150\,\mathrm{ps}$ and a position resolution of $1.5\,\mathrm{cm}$ for flight paths in the range from $10\,\mathrm{m}$ to $35\,\mathrm{m}$ [10].

The remaining two arms are specifically designed for charged particles like protons, deuterons, alphas, and heavier ions that are susceptible to deflection by the magnetic field. For a given value of the magnetic field, the amount of deflection each particle suffers is solely dependent on its magnetic rigidity, the higher it is the less deflection the particle will suffer. **Magnetic rigidity** is a property of every charged particle, defined by the ratio of its mass (proportional to the atomic number, A) and its charge (Q). For the same energy per nucleon, heavier ions have a higher magnetic rigidity, making them less likely to bend in the magnetic field compared to lighter particles. This necessitates two separate arms: one for protons, with an A/Q of 1, and another for heavier ions, which have an A/Q greater than 1. Deuterons and alphas, for example, have an A/Q of 2, resulting in half the deflection protons suffer.

The set of detectors used to track particles with magnetic rigidities greater than 1, changes depending on the requirements of the experiment. Currently, the setup is composed of fibers and a Time Of Flight Detector (TOFD) [11].

The last of the three arms is the proton arm responsible for the detection of particles with less magnetic rigidity, like protons. This arm is where the current Resistive Plate Chamber (RPC) detector has

been installed, allowing for the measurement and characterization of the high-energy produced protons. The high efficiency and time properties for the detection of these particles during the recently executed campaign will allow the extraction of precise knowledge of the reactions under study [12].

At the heart of the R^3B experimental setup, surrounding the reaction target, is the CALorimeter for In-Flight detection of gamma-rays and high-energy charged pArticles (CALIFA), the calorimeter of the experiment [13–19], which aims at the detection of very energetic photons and light charged particles that are radially emitted during the reaction and do not enter GLAD.

1.2 Calorimeters

Calorimeters are detectors used to reconstruct the momenta of particles and are commonly used in a wide variety of fields like in high-energy physics experiments [20], nuclear physics [21], and astrophysics and cosmology [22], as well as in material science [23]. They work by completely absorbing all the energy of a particle, utilizing dense materials such as lead, iron, or scintillating crystals [24], that after absorbing the energy of the particle, convert it into measurable phenomena like heat, ionization, or light. In low-energy experiments [25], in the below the few MeV per nucleon regime, the incoming particles may not have enough energy to ionize or even excite the particles of the material. In these cases, heat is often used as the measurement mechanism using sensitive thermometers to detect the slightest amount of heat generated by the interaction of the particles with the detector's active material. In high-energy physics, experiments involving particles with energies above a few MeV per nucleon, a different approach is often used. Detectors using scintillators or sampling calorimeters are favored due to their faster response times and ability to handle high particle fluxes. Due to the relativistic velocities of particles at R^3B, experiments operate in the high-energy regime, and so, a scintillator-based calorimeter was chosen.

Scintillators

Scintillators are materials (solids, liquids, or gases) that produce sparks or scintillations of light when struck with ionizing radiation. This light can then be measured by various readout devices. Traditionally, Photomultiplier Tube (PMT) have been used, which amplify the light and convert it into a read-out signal via the **photoelectric effect**. More recently, devices such as Silicon Photomultipliers (SiPMs), Photodiodes (PDs), and Avalanche Photodiodes (APDs) have also been employed for their compactness, robustness, and improved performance in specific applications. There are a few types of scintillators that have been developed to exploit this phenomenon for diverse applications. These are organic scintillators, inorganic scintillators, and gaseous scintillators [26].

- **Organic crystals** are composed of organic materials that provide detectable photons in the visible range of the light spectrum. The scintillation mechanism in organic materials is the result of molecular transitions. Organic scintillators comprise crystalline, liquid, plastic, and glassy forms. Although organic scintillators have a faster decay time, around 10^{-8} seconds compared to the 10^{-6} seconds of inorganic scintillators, they generally produce a lower light output and interact less strongly with X-rays and gamma rays than inorganic scintillators. This makes them better suited for applications that involve large volumes, neutron detection, and very fast timing characteristics.

- **Inorganic crystals** are made from inorganic compounds or ceramic materials. Scintillation in inorganic crystals is typically slower than in organic ones. They exhibit high efficiency for the detection of gamma rays and are widely used for the identification of ionizing radiation isotopes via gamma-ray spectroscopy. Inorganic scintillators are better at detecting gamma rays and X-rays than organic scintillators due to their high density. A disadvantage of some inorganic crystals is their hygroscopicity, a property that requires them to be housed in an airtight container to protect them from moisture. Inorganic crystals are also more expensive than organic scintillators.

- **Gaseous scintillators** use noble gases like helium as the scintillating medium. The scintillations are produced as a result of atomic transitions. Since the light emitted by noble gases belongs to the ultraviolet region, other gases, such as nitrogen, are added to the main gas to act as wavelength shifters. They offer a very short decay time, but require a specialized gas handling system and have a low efficiency for gamma detection. These features make them suitable for the energy measurement of heavy charged particles (alphas, fission fragments, other heavy ions) [27].

For R^3B experiments, the calorimeter needs to measure very energetic photons and light particles, making inorganic scintillators the most viable option for this physics case.

Inorganic Scintillators

There are several types of inorganic scintillators, including alkali halides, Čerenkov crystals, and oxide crystals. Each type offers unique properties that make it suitable for specific applications. To be considered a good inorganic scintillator [28], the crystal must possess several key properties:

- **High density**: The higher the density, the better the stopping power of the scintillator and the better efficiency in converting the kinetic energy of particles into light.

- **Light output**: The amount of photons emitted per energy unit. A higher light output leads to a better output signal and higher resolution.

- **Linearity**: so that the increase in light output is proportional to the energy deposited being better for signal conversion.

- **Sensitivity peak**: Is the wavelength at which the crystal emits the maximum amount of light. Crucial to calibrate the photomultipliers and obtain the best resolution.

- **Decay time**: a fast response to events and a low dead time are necessary for high rates of measurement.

- **Hygroscopicity**: A hygroscopic crystal absorbs humidity from the air, degrading its performance. So the less hygroscopic the better.

- **Radiation length**: The distance over which a high-energy electron loses approximately 63% of its initial energy. Shorter radiation lengths mean the material is more effective at absorbing electromagnetic radiation

Table 1.1 provides a direct comparison of various inorganic crystals that were considered for CALIFA calorimeter [13], highlighting their key properties.

Table 1.1: Main properties of different scintillator materials. Taken from [13].

Material	CsI(Tl)	$LaBr_3$(Ce)	$LaCl_3$(Ce)	NaI(Tl)
Density ($g/cm3$)	4.51	5.29	3.86	3.67
Light Output (photons/MeV)	52k	63k	49k	39k
$\Delta E/E$ (% at 662 keV, PMT)	6	3	3.5	7
Sensitivity peak (nm)	550	380	350/430	310/415
Decay constant (ns)	700/3300	25	25/213	620/230
Hygroscopic	Slightly	Yes	Yes	Yes
Radiation Length (cm)	1.86	1.881	2.813	2.59

1.2.1 CALIFA Geometry

CALIFA is positioned around the target chamber and covers the polar angles between 7º and 140.3º. It is highly segmented containing 2544 crystals. CALIFA is separated into two sections, the **Barrel** and the **Forward Endcap**, see Figure 1.2.

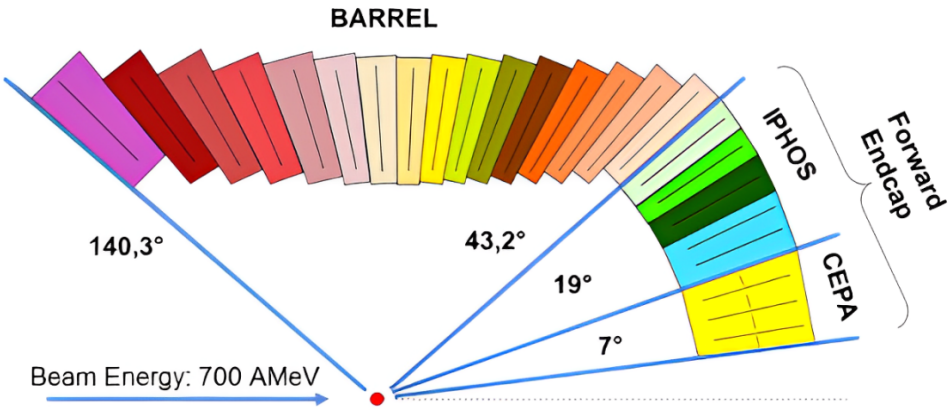

Figure 1.2: Schematics of CALIFA with a cut on the side view. There can be seen the two main sections that are part of CALIFA, the barrel and the forward endcap. The forward endcap is further divided into the IPHOS and CEPA parts. Image adapted from [14].

Barrel

The barrel section is comprised of 1952 crystals of Thallium-activated Cesium Iodide (CsI(Tl)) with lengths that range from 12 cm to 22 cm and are shaped like an asymmetric frustum of a pyramid, creating a cylindrical pattern around the beamline and cover the polar angles between 43º and 140º. It covers the angular range necessary to overcome limitations imposed by the Doppler broadening that occurs at high beam energies that approach 1 AGeV and meets the challenging demands imposed by the wide physics

range of the R^3B experiment program which requires both the detection of low-energy γ-rays from single-particle excitations and high-energy γ-rays associated with different collective modes, in addition to the detection of charged particles emitted from the reaction zone.

Forward Endcap

The forward endcap is responsible for the coverage from 7º to 43.2º. It is further divided into two sub-sections, the **intrinsic Phoswich (iPhos)** [29] and the **CALIFA Endcap Phoswich Array (CEPA)** [30]. The iPhos section covers the range of angles between 19º and 43.2º while the lower angles, 7º to 19º, are covered by CEPA.

CEPA is the section of CALIFA that is specifically designed to handle the most energetic and intense light-charged particles and gamma rays. For that, the original design used Cerium-doped Lanthanum Bromide ($LaBr_3(Ce)$), and Cerium-doped Lanthanum Chloride ($LaCl_3(Ce)$) crystals, for their fast response time, needed in a high-intensity environment. However, this concept was not operationally possible and different options are currently under investigation like the combination of GAGG and CsI crystals in a phoswich configuration. For a temporary solution the same CsI(Tl) crystals are being used.

When a collision happens, the heavy ions will follow an almost linear path entering GLAD, while light-charged particles like protons or light nuclei, can be dispersed in other directions. The most energetic particles, reaching energies as high as $700\,\mathrm{MeV/u}$ are predominantly emitted in the forward direction, entering the CEPA region. The length of the crystals composing CEPA is not long enough to fully stop the most energetic particles and they will punch-through the detector. This limitation has two consequences: the energy of the particles cannot be determined with the precision it should have (below 1% [2]) and discrimination among isotopes of the same atomic element cannot be done, as they have similar energy deposited in the crystal.

1.3 The RPC solution

The present thesis proposes the design and benchmarking of an RPC detector, for the detection of the light-charged particles that punch-through CALIFA and is to be implemented behind the forward endcap of CALIFA. This work not only builds upon the established principles of RPC-based particle detection but also extends its scope to encompass all the different physics programs that are held in the R^3B setup, thereby advancing the comprehension of particle interactions in complex nuclear systems. The design of the detector should be optimized for the measurement of protons, deuterons, and alpha particles from the induced reactions. Simulations of the detector were performed using the R3BRoot framework, allowing for the implementation of future detection systems in the R^3B experimental environment. The results from these studies should promote the decision to build and implement a prototype of this detector for the upcoming experimental campaigns.

The following sections investigate the theoretical aspects of RPCs and their symbiotic relationship with the R^3B/FAIR experimental framework. The methodologies employed to simulate and analyze the interactions of protons, deuterons, and alpha particles are exposed, followed by the presentation and interpretation of simulation results. The innovative concept proposed here not only strives to enhance

the accuracy and precision of particle measurements but also contributes to the broader understanding of nuclear physics phenomena.

The challenges presented by the experimental program of the R^3B collaboration open an opportunity to explore the improvement of the existing systems and, consequently, the extraction of complementary and more precise information from the reaction processes under study. To effectively conduct the proposed RPC study effectively, it is essential to address several key points to achieve the intended goals. The optimization of the design for the measurement of high-energy light-charged particles will be based on the existing RPC at R^3B. The altered design must be implemented within the R3BRoot simulation framework for comprehensive testing and analysis and perform simulations in conjunction with the CALIFA detector to effectively understand their combined response.

1.4 PAS Concept

The Proton-Arm Spectrometer (PAS) is a key part of the R^3B experiment, mainly to detect protons and high velocities light-charged particles. The goals for the PAS concept are to obtain a momentum resolution lower than 0.1%, a position resolution lower than $150\ \mu m$, and $1\ \mathrm{mrad}$ of angular resolution. Initially, the PAS design included Straw-Tube Walls (STW) detectors that would cover a ± 80 *mrad* acceptance range [31]. This setup had four detectors with three layers of straw tubes each, providing position information in two dimensions for full proton track reconstruction. The first STW used Mylar tubes, while the others were planned with aluminum tubes to save on cost and deal with technical problems, achieving an angular resolution of less than $0.3\ \mathrm{mrad}$.

Originally, the PAS project was an in-kind contribution from Russia, with construction and testing undertaken by the Petersburg Nuclear Physics Institute (PNPI). However after the Russian contracts were canceled in 2022, the project had to be redesigned using technologies available to the R3B collaboration. So, finding another method was necessary. Simulations were conducted using different setups that utilized RPCs and fibers. These simulations aimed to explore various design possibilities to ensure that PAS met the requirements of the R3B experiment. Further details and results of these simulations will be discussed in chapter 5.

Chapter 2

Energy Loss Mechanisms

In this chapter, it will be discussed the theoretical mechanisms of energy loss of particles in material and particle detectors. Based on references [27, 32].

In the field of experimental nuclear physics, where fundamental particles collide with each other, the main interest is the results of the reactions that occur. It is therefore essential to detect such particles allowing the reconstruction of the event. While the specific detectors used for these measurements differ according to the type of particle being detected, they are all based on a common principle: their operation relies on the amount of energy the particle deposits within their active material. So it is essential to understand how different particles lose their kinetic energy when interacting with atomic matter. These processes are complex and involve quantum mechanics, electromagnetism, and the nuclear strong force. These mechanisms depend on the type of particle detected for charged particles, neutrons and photons all have different energy loss processes associated with them.

2.1 Energy Loss Mechanisms of Neutrons particles

Neutrons do not interact with electrons via the electromagnetic force (Coulomb interaction) because of their neutral charge. This allows them to penetrate deeper into the matter before interacting with atomic nuclei, a process dominated by the much stronger, but short-range, nuclear force. While nuclear interactions are more likely for neutrons compared to charged particles, their short range ($\approx 10^{-13}$ cm) still makes them a rare phenomenon.

When an interaction does occur, the neutron energy determines the nuclear process most likely to suffer. These processes can be divided into two categories: **scattering** and **absorption**.

Scattering

In a scattering interaction, the neutron interacts with a nucleus, and both particles reappear after the reaction. They are either elastic or inelastic.

- **Elastic scattering** from nuclei, A(n, n)A: This is the most relevant mechanism of energy loss for neutrons in the $\mathrm{MeV/u}$ region.

- **Inelastic scattering**, A(n, n')A*, A(n, 2 n')B: In this reaction, the nucleus is left in an excited state which may later decay by γ-ray or some other form of radiative emission. For the inelastic reaction to occur, the neutron must have sufficient energy to excite the nucleus, usually on the order of $1\,\mathrm{MeV/u}$ or more. Below this energy threshold, only elastic scattering may occur.

Absorption

If the interaction is an absorption, the neutron disappears, but one or more other particles appear after the reaction takes place.

- **Radiative neutron capture**: the neutron is captured by the nucleus releasing energy (n+(Z, A) $\longrightarrow$ γ+(Z, A+1)). In general, the cross-section for neutron capture goes approximately as $1/v$ where v is the velocity of the neutron, and so absorption is most likely at low energies.

- **Other neutron induced reactions**, such as (n, p), (n, d), (n, a), and others: the neutron is captured and charged particles are emitted. These generally occur in the eV to keV region. Like the radiative capture reaction, the cross-section generally falls as $1/v$.

- **Fission**, $n + {}^{A}_{Z}X \longrightarrow {}^{A_1}_{Z_1}Y_1 + {}^{A_2}_{Z_2}Y_2 + n + n + ...$: when a neutron collides with a heavy atom (like uranium or plutonium) above a certain energy threshold, the nucleus can become unstable and split into two smaller nuclei (fission products) along with a burst of energy and additional neutrons. These released neutrons can then go on to cause fission in other heavy atoms, creating a chain reaction that releases enormous amounts of energy.

2.2 Photons

Photons, also referred to as x-rays and γ-rays, interact with matter in several ways. The three most relevant ones are: **Photoelectric Effect**, **Compton Scattering**, and **Pair Production**.

These reactions account for the two main qualitative characteristics of x-rays and γ-rays: first, they penetrate matter deeper than charged particles, and second, a beam of photons is only reduced in its intensity instead of its energy, traveling through a layer of matter. The first feature results from the three processes having a substantially smaller cross-section compared to the cross-section of inelastic electron collisions. The second feature, on the other hand, results from the photon being completely removed from the beam by either scattering or absorption in the three mentioned processes. Therefore, the photons that pass through without encountering anything are the ones that have not experienced any interactions at all. As a result, they keep their initial energy.

Photoelectric Effect

The interaction between a photon and a bound atomic electron is the photoelectric effect. In this interaction, the photon is absorbed and one of the electrons is ejected as a free electron. The kinetic energy of this ejected electron is:

$$T = E_\gamma - B_e \tag{2.1}$$

where E_γ is the energy of the incident photon and B_e is the binding energy of the electron. The *photoelectric cross-section* is given by:

$$\tau(m^{-1}) = aN_a \frac{Z^n}{E_\gamma^m}[1 - O(Z)] \tag{2.2}$$

where:

$\boldsymbol{\tau}$: is the probability for the photoelectric effect to occur per unit distance traveled by the photon.

$\boldsymbol{a}$: is a constant, independent of Z and E_γ.

$\boldsymbol{m}$, $\boldsymbol{n}$: are constants with a value of 3–5 (their value depends on E_γ).

$\boldsymbol{N}$, $\boldsymbol{Z}$: are the Avogadro's number and the atomic number of the material, respectively.

$\boldsymbol{O(Z)}$: are first order corrections in Z.

Equation 2.2, shows the dependence of this cross-section on the parameter E_γ, Z, and A. The interaction is more probable in nuclei with higher atomic numbers, and also for lower values of the photon's energy.

Compton Scattering

When a photon collides with a free electron both suffer deflection. This is called the *Compton scattering* or *Compton effect*. Under normal circumstances, all the electrons in a medium are bound. However, the Compton effect is still relevant if the energy of the photon is of the order of keV or higher while the energy of the bound electron is generally in the eV range. In these conditions, the electron may be considered free. Figure 2.1 shows the schematics of the interaction.

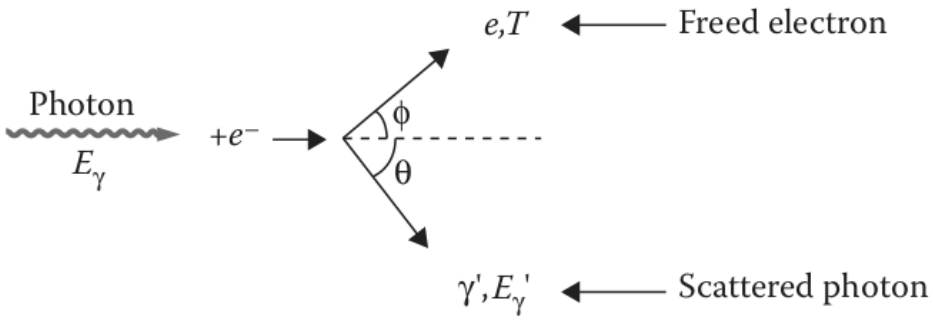

Figure 2.1: Trajectory of the photon and particle undergoing Compton scattering.[27].

In contrast to the photoelectric effect, the photon does not disappear after a Compton scattering. It merely changes direction and energy. So (assuming the electron is stationary before the collision), the conservation of energy gives:

$$T = E_\gamma - E_{\gamma'} \tag{2.3}$$

Conservation of momentum gives us that $E_{\gamma'}$, as a function of θ, is (see [33]):

$$E_{\gamma'} = \frac{E_\gamma}{1 + (1 - cos(\theta))E_\gamma/mc^2} \tag{2.4}$$

Using equation 2.4 in 2.3, the kinetic energy of the scattered electron is:

$$T = \frac{(1 - cos(\theta))E_\gamma/mc^2}{1 + (1 - cos(\theta))E_\gamma/mc^2} E_\gamma \tag{2.5}$$

The *Compton cross-section* can be written in the form:

$$\sigma(m^{-1}) = NZf(E_\gamma) \tag{2.6}$$

where σ is the probability for Compton interaction to occur per unit distance and $f(E_\gamma)$ is a function of E_γ. This cross-section decreases as the energy of the photon, E_γ, increases, and stays approximately constant with the increase of the atomic number Z.

Pair Production

Pair production is a process where a high-energy photon interacts with the strong electric field of an atomic nucleus and creates an electron-positron pair.

Through conservation of energy, the kinetic energy of the electron and the positron is:

$$T_e + T_{e^+} = E_\gamma - (mc^2)_{e^-} - (mc^2)_{e^+} = E_\gamma - 1.022MeV \tag{2.7}$$

Equation 2.7 reveals that the minimum energy of the photon necessary to produce an electron-positron pair is $1.022\,\mathrm{MeV}$. If the energy of the photon is higher than this value, it will translate into kinetic energy for the resulting pair.

The pair production cross-section is a function that depends on E_γ and Z. Out of the three processes described, pair production is the only one where the cross-section increases with the photon's energy.

2.3 Charged particles

Charged particles are any particles that have an electrical charge. They can be light particles, electrons (e^-), and positrons (e^+) or heavier particles like protons, deuterons, alphas, and all of the particles with $A > 4$. They interact primarily through Coulomb forces. This interaction translates into two principal features that characterize the passage of charged particles through matter: the loss of energy by the particle and the deflection of the particle from its incident direction. The particle's penetration range depends on three factors: the type and energy of the incident particle and the material it is passing through.

Electrons (e^-) and positrons (e^+) should be treated separately from charge particles with atomic numbers greater than one. This comes from the high probability of electrons undergoing inelastic collisions with atomic nuclei resulting in significant kinetic energy transfer in a single interaction. This process, often ionization, leads to a characteristic "zig-zag" trajectory due to frequent, large-angle scattering by the atomic electron cloud. Additionally, at relativistic energies, bremsstrahlung emission becomes a significant energy loss mechanism for electrons, as they emit electromagnetic radiation when deflected by the electric field of nuclei. On the contrary, heavier charged particles like protons (p^+) or muons (μ^-) have a significantly larger rest mass ($m_p \approx 1.67 \times 10^{-27}$ kg, $m_\mu \approx 1.88 \times 10^{-25}$ kg), which translates to a smaller fraction of the energy being transferred per collision with atomic electrons, resulting in a more gradual reduction in kinetic energy. Additionally, the larger inertia of heavier particles makes them less susceptible to deflection by the Coulomb force exerted by atomic electrons. Consequently, heavier charged particles exhibit a straighter and deeper trajectory into the material, compared to their lighter counterparts.

In this thesis, the particles studied are protons, deuterons, and alphas and not electrons. So, the focus will be directed to these particles.

Although much less probable in the energy range we are considering, there are other energy loss mechanisms besides the Coulomb forces, that contribute to energy loss of charged particles. These are:

- Emission of Čerenkov radiation;
- Nuclear reactions.

Energy Loss by Coulomb Interactions

Coulomb interactions are a process in which charged particles are deflected due to their electrostatic interactions with the positively charged nuclei of target atoms, resulting in either elastic or inelastic scattering. The schematics of the process can be seen in Figure 2.2:

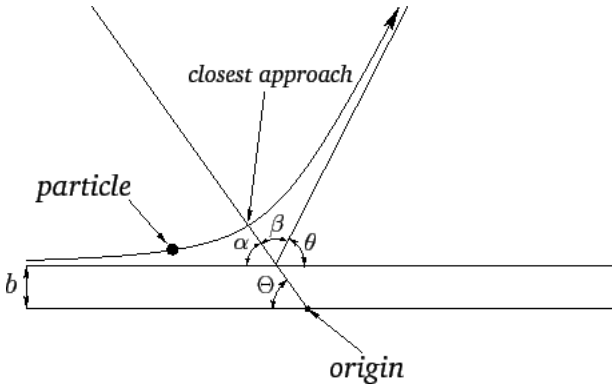

Figure 2.2: Trajectory of the particle undergoing Coulomb scattering. Showing the closest approach point, the scattering angle θ and b, the *impact parameter* [34].

Elastic collisions, or Coulomb scattering, is a process where the total energy involved is conserved in the momenta of the particles, meaning that the scattering event does not excite or ionize the atoms

involved. This process is more relevant at energies close to their rest mass energy. At higher energies are not so relevant and can be neglected.

In **inelastic** Coulomb scattering, some of the incident particle's energy is transferred to the atom, exciting or ionizing the target atom.

The **ionization** process happens when an atom loses an electron. This usually occurs when a fast-moving charged particle, often an electron or an ion, has high enough energy and transfers some of it to an atomic electron causing it to become detached from its original atom, creating a positively charged ion (cation) and a free electron, as described in 2.8 (μ^+ is the relativistic charged particle). The electron freed from the atom acts like any other moving charged particle. It may also cause ionization of another atom provided its energy is high enough. It will stop after interacting with matter. Fast electrons produced by ionizing collisions are called δ-rays. The energy required for ionization is specific to the atom and is called the ionization energy. Following the periodic table Figure, 2.3, the energy required to ionize an atom increases from left to right within a period and decreases along a group.

$$\mu^+ + atom \longrightarrow \mu^+ + atom^+ + e^- \tag{2.8}$$

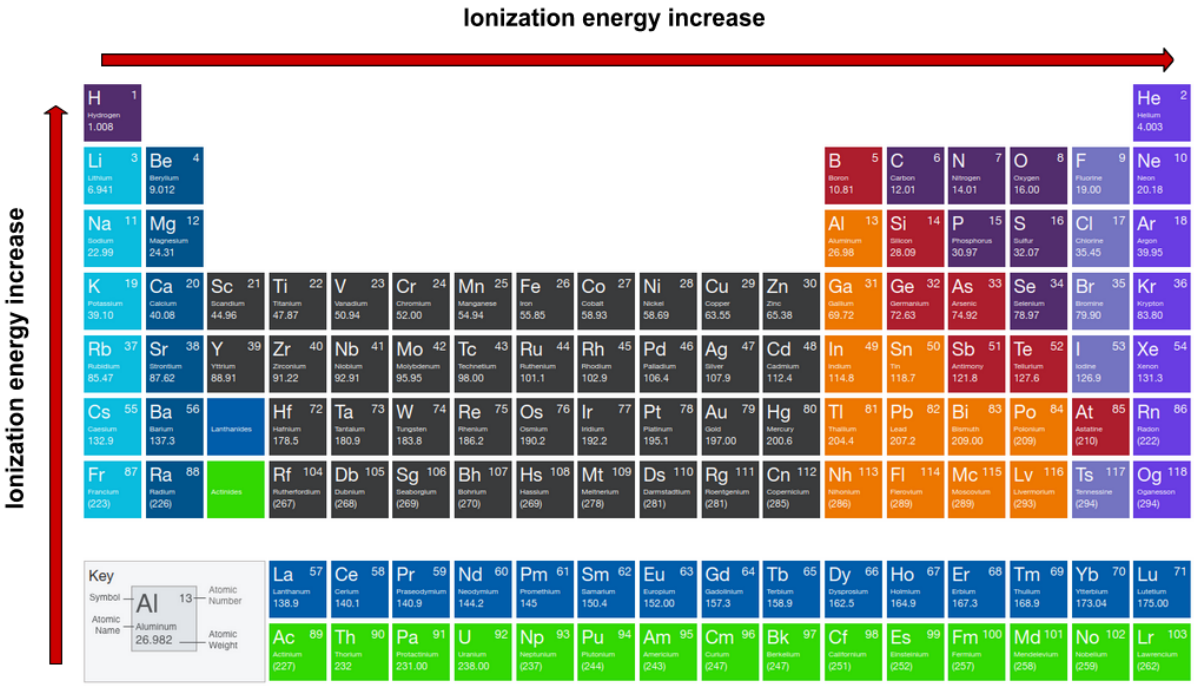

Figure 2.3: The Periodic Table of Elements. The energy needed for ionization increases along the groups and decreases along the periods [35].

Excitation, on the other hand, occurs when the incident particle leaves enough energy on an atomic electron taking it to a higher energy state within its orbital, but not enough energy to ionize it. This transition is temporary and the excited electron eventually returns to its original state. The excess energy is released in the form of electromagnetic radiation (photons) or transferred to the surrounding lattice as vibrational energy (phonons), which can manifest as heat. The energy threshold for excitation is lower

than that for ionization, and the probability of excitation depends on the incident particle's energy and the target atom's properties. See Figure 2.4 for the energy loss relative to excitation and ionization in different materials for 3 incident particles: Muon, Pion, and Proton.

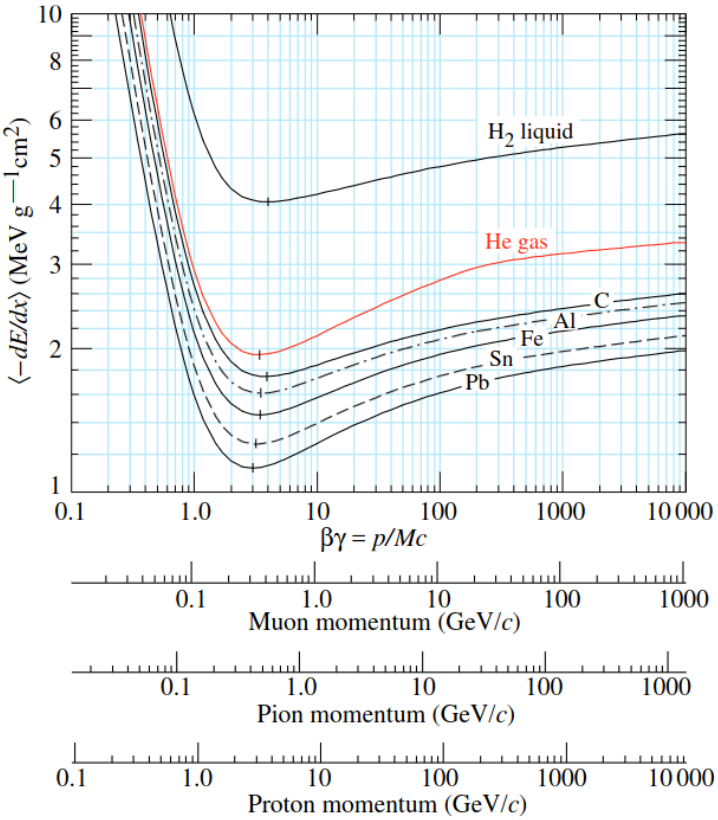

Figure 2.4: Energy loss due to ionization and excitation in different materials, liquid hydrogen, helium gas, carbon, aluminum, iron, tin and lead [36].

Bethe-Bloch Formula

The relationship between a particle's energy and its penetration depth within a material, also known as its range, can be described by the Bethe-Bloch formula. This formula, derived by Hans Bethe in 1930, provides the average energy loss per unit path length experienced by a charged particle traversing a material, also known as the stopping power (S). While more sophisticated approaches exist, the Bethe-Bloch theory for electronic stopping power remains widely used due to its simplicity and effectiveness [37].

The Bethe-Bloch formula relies on the first Born approximation, assuming the stopping power arises primarily from Coulomb excitation and ionization of target atoms by the projectile.

The simplified Bethe-Bloch formula can be expressed as:

$$-\frac{1}{\rho}\frac{dE}{dx}\bigg|_{col} = \frac{C}{\beta^2}\frac{N_A}{A}\left[ln\frac{2m_e c^2\beta^2\gamma^2 E_{max}}{I^2} - 2\beta^2 - \delta\right] \tag{2.9}$$

where:

- ρ is the density of the material that is transversed
- dE/dx is the rate of energy loss (col term indicates collisional processes)
- C is a constant defined by $C = 2\pi Z z^2 r_e^2 m_e c^2$ [MeVcm^2]
- β is the beta factor, the velocity of the particle relative to the speed of light (v/c)
- N_A is Avogadro's constant
- A is the atomic mass of the target material
- E_{max} is the maximum transferable energy in a single collision
- I is the mean excitation energy of the target atom
- γ is the Lorentz factor $(1/\sqrt{(1-\beta^2)})$
- δ is a density correction term

The key terms in this equation are the logarithm term, describing the energy loss due to collisions with target electrons and the terms with β^2 account for relativistic effects, where energy loss increases with particle velocity.

However, the Bethe-Bloch formula in 2.9 has limitations, particularly at low particle velocities. It assumes the projectile (ion) carries no atomic electrons. In reality, if electrons are present, they can shield the ion's nuclear charge, reducing its interaction with the target material and its energy loss. Additionally, the formula focuses solely on electronic stopping power. Nuclear stopping power, arising from interactions with the atomic nucleus, is another component of total stopping power.

Equation 2.11, is a version of the Bethe-Bloch formula that has into account several terms that make it more reliable [38].

$$S = \frac{4\pi {Z_1}^2 e}{m_e v^2} N Z \left\{ ln\left(\frac{2m_e v^2}{I_0'}\right) + ln\gamma^2 - \beta^2 + \frac{1}{2} f(\gamma) \right. \tag{2.10}$$

$$\left. + \frac{S_0 - Z}{2Z}[ln(\beta^2\gamma^2) - \beta^2] - \frac{C(\gamma)}{Z} - \frac{1}{2}\delta_F + \Delta L^{LS} + \Delta L^B(a) \right\} \tag{2.11}$$

These corrections are:

- Shell correction (S_0): accounts for the energy required to excite or ionize electrons in different shells of the target atom.
- Density effect correction ($f(\gamma)$, δ_F): considers the influence of the target's material density on electronic stopping power.
- Barkas correction ($C(\gamma)$): Accounts for relativistic effects at high particle velocities.

- Lindhard-Sørenson correction (ΔL^{LS}): Improves accuracy by considering the collective response of target electrons to the projectile.
- Bloch correction ($\Delta L^{B}(a)$): Accounts for the finite size of the target atom, which becomes important at low particle velocities.

2.3.1 Radiation loss-Bremsstrahlung

Charged particles, like electrons or protons, traveling at relativistic speeds experience a phenomenon called radiation loss. This occurs when the charged particle interacts with the electric field of atomic nuclei in a material. As the particle travels through the material, it undergoes numerous deflections due to these interactions. These deflections cause the particle to lose some of its kinetic energy, which is emitted through electromagnetic radiation (photons) like X-rays or gamma rays. This radiation is called bremsstrahlung, which is German for braking radiation

The intensity of the emitted radiation I is proportional to the square of the particle acceleration, which in turn is dependent on the charge (ze) and mass (M) of the moving particle and the atomic number of the material (Z), and are related through the Coulomb force $F \approx zeZe/r^2$, r being the distance between the two charges. The acceleration of the incident charged particle is $a = F/M$. We have:

$$I \propto a^2 \approx (\frac{zZe^2}{M})^2 \approx \frac{z^2Z^2}{M^2} \tag{2.12}$$

The amount of radiation loss depends on several factors. The closer the particle gets to the nucleus (smaller distance of closest approach), the stronger the electric field and the greater the deflection, resulting in a more significant radiation loss. Additionally, particles traveling closer to the speed of light (higher β) experience a stronger radiation effect due to relativity. Finally, the atomic number (Z) of the target material plays a role. Materials with heavier nuclei (higher Z) have a stronger electric field, leading to a more pronounced radiation loss for the charged particle.

2.3.2 Čerenkov Radiation

When a charged particle, typically an electron or a proton, transverses a material with a velocity greater than the velocity of light in that material, it emits Čerenkov radiation with a characteristic angle Θ, dependent on the velocity of the particle and the speed of light of the material, forming a light cone.

$$cos(\Theta) = \frac{1}{n\beta} \tag{2.13}$$

The energy loss associated with this process is negligible in most cases, but it can be used to do particle identification, for different particles have different masses and therefore different velocities to produce Čerenkov radiation. One example of a detector that uses this phenomenon to identify particles is the Ring-Imaging Čerenkov Detector (RICH) [39] present at Large Hadron Collider (LHC) [40].

Chapter 3

Ionization detectors and Resistive Plate Chambers

In this chapter, it will be discussed the functioning principles of detectors, with a focus on RPCs. The RPC text is based on [41] and [42].

3.1 Charged Particles Detection Techniques

High-energy physics experiments generally focus on collisions between particles. There are two primary methods for these collisions. One involves colliding two beams, as it is done at CERN [43], where two particle beams are accelerated to nearly the speed of light and collide in opposite directions. This method maximizes the energy available in the center-of-mass frame, making it highly efficient for studying high-energy interactions. The other method uses a beam and a static target, a process that is employed at R^3B. This beam is accelerated to high speeds and directed at a stationary target. This method has the downside of lowering the total energy available in the center-of-mass frame, but in turn allows for more precise control over the experimental setup, as the target is fixed and stable, simplifying the collision geometry and analysis, compared to the beam-beam collision.

In either method used, it is necessary to use many systems of detectors to analyze the reactions produced. Each detector is designed to perform a set of tasks.

There exist several types of working principles for these charged particle detectors, that go under two main types: Solid-state detectors, like scintillating, semiconductor, and Čerenkov counters, and Gaseous ionization chambers such as a Geiger-Müller tube, ionization counters, and spark chambers. The RPC is an example of an ionization-type detector.

3.2 Ionization Detectors

One of the first gas detectors with the application of strong uniform electric fields to parallel plates, was the Keuffel Spark Counter in 1948 [44]. The main interest of Keuffel was to make a detector with a time resolution better than the one available at the time, provided by the Geiger-Müller Counter, around the $100\mu s$ [45]. With the new detector, Keuffel reduced the time resolution to $1\,\mathrm{ns}$, an improvement good enough to develop accurate timing systems and measure the velocity of fast-charged particles.

Spark counters work by having two parallel metal electrodes (copper in Keuffel's detector), with high voltage applied to them, and the gap between the plates is filled with a gas. The gas is responsible for the creation of the free charge carriers (electrons) when a charged particle passes through. This trail of charged particles in conjunction with the electric field applied, creates avalanches of charge carriers. These avalanches can transform into streams after a certain size, which is a point where photons start to play an important role in the spread of free-charge carriers. These streamers then create a plasma filament that connects the two electrodes, creating an electrical discharge, giving it the name spark counter. This discharge is then read as an electrical signal and marks the particle's arrival.

Using streams for time measurements has its advantages and disadvantages. For one, it leads to large signals that can be easily read, making electronic amplification unnecessary, and leading to less electronic noise. But this large stream also means that the charge will spread for a larger surface area, producing a large position resolution, which is not ideal for tracking. Also, parallel-plate counters are not capable of high counting rates, because the large discharges that the streams create, provoke large quenching times (0.01 to 0.05 s), meaning that if two streams hit the same place in a very short amount of time, they are not distinguishable. This is called *dead time*, which is the time necessary to recharge the electrodes.

To fix these problems, a new type of detector was introduced, called resistive plate electrodes, and had plates with resistivities of around $10^9\ \Omega cm$. In these detectors, the spread of the streams is smaller and more precise. New gas mixtures were also developed for better photon absorption. The Pestov Spark Counter is an example of a detector that had this improvement. It was a detector developed for the ALICE Experiment at GSI [46], and it was a single-gap, gaseous parallel-plate detector, that operated in streamer/spark mode. Due to the gas mixture, it was able to keep the discharge local, reducing the dead area from a few cm^2, to below $2\,\mathrm{mm}^2$. Also, having a gas gap of about $0.1\,\mathrm{mm}^2$, made it possible to have a time resolution as low as $25\,\mathrm{ps}$.

Another type of detector is the Parallel-Plate Avalanche Chambers (PPAC), developed first in 1952 but only popularized in 1975 when they started being used to detect heavy ions [47]. It is very similar to the spark counter, but instead of being operated in streamer mode, operated in avalanche mode. These detectors are capable of a $250\,\mathrm{ps}$ time resolution [48].

3.3 Resistive Plate Chamber

The Resistive Plate Chamber (RPC) was introduced in 1981 by R. Santonico and R. Cardarelli [49] as a practical alternative to localized discharge spark counters. The RPC is essentially based on the same principles as Pestov's Spark Counter with innovations that simplify the production and utilization of this type of detector. These include the absence of high-pressure gas and lower requirements of mechanical precision. The resulting detector was free from damaging discharges and provided a time resolution of the order of $1\,\mathrm{ns}$, a value that has been improved since it first appeared. Together, these merits made RPCs of potential interest in a different and wider range of applications in modern experiments, becoming a cost-effective alternative to plastic scintillators for whenever large area detectors in low counting rate environments are needed.

An RPC is a gaseous particle detector that utilizes a uniform electric field generated by a parallel

plate electrode (some RPCs can have more than 2 plates). At least one of these plates is made from a highly resistive material, generally between 10^{10} and 10^{12} Ωcm. The gap between the plates is filled with a specific gas mixture to ensure high ionization efficiency and absorb ultraviolet light. A thin layer of graphite is coated over the external surface of the electrodes to allow a uniform application of the high voltage. See Figure 3.1 for a schematic of a one-gap RPC.

When a charged particle traverses the chamber, it ionizes the gas and creates free charges. These free charges create avalanches of electrons within the electric field, leading to a detectable signal. The high resistivity of the electrodes confines the temporary decrease of the electric field to a small region around the initial avalanche preventing the discharge from spreading throughout the gas volume and maintaining sensitivity in unaffected areas. On the other hand, the capacity of the gas to absorb ultraviolet light, means the photons produced by the discharge are incapable of propagating in the gas. This prevents secondary discharges from originating at other points in the detector. The propagation of the growing number of electrons induces a current on the external strip electrodes.

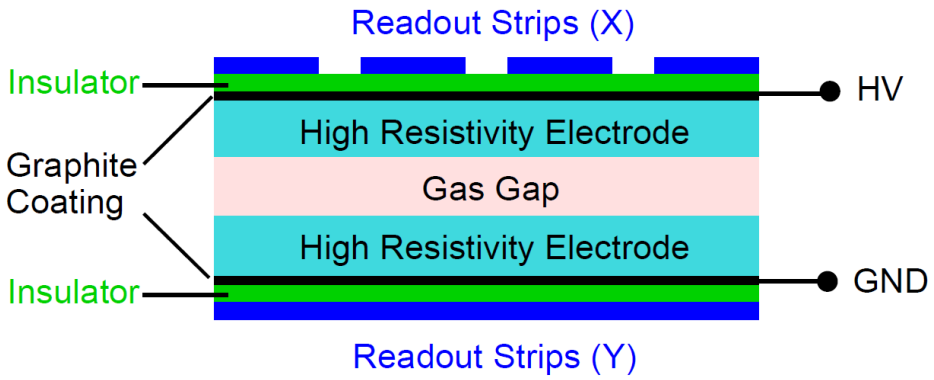

Figure 3.1: The basic schematic view of a one-gap RPC. [42]

Depending on the settings of the RPC, they can exhibit much better time resolution than wire chambers or limited streamer tubes, in the few tens of picoseconds. This advantage arises from the uniform field used, instead of the field created by the wire chambers, that are dependent on $1/r$ (r being the distance to the wire), which introduces large time fluctuations due to the electron drift velocity. More sophisticated versions of RPCs exist, in which extremely flat electrodes of semi-conducting glass, and high-pressure gas were utilized and also Multigap Resistive Plate Chamber (MRPC) [50, 51]. These detectors provide time resolutions considerably better, even better than those attainable by scintillators.

Operation modes

RPCs may be operated either in avalanche or streamer mode (also known as discharge mode). Figure 3.2 shows a schematic of the avalanche formation process. Firstly a particle hits the detector, ionizing some gas molecules. These primary ionization electrons gain sufficient energy from the electric field to, in turn, ionize other gas molecules creating secondary electrons. The resulting secondary electrons then produce tertiary ionization and so on, constituting a Townsend avalanche. With a gas gain large enough, the avalanche reaches a point of self-sufficiency, meaning the avalanche charge carriers influence the

electric field in the gas gap and so their propagation and multiplication (the *space charge effect*). The drift velocity of electrons is much higher than the ions, so they reach the cathode much faster, while ions take longer to reach the anode. The charges in the resistive electrodes close to the avalanche influence the electric field, lowering it locally.

When operated in avalanche mode (streamer formation is suppressed), RPCs offer significantly improved counting rate capability. This is typically achieved by changing the characteristics of the gas mixture, like adding small amounts of SF_6 to the gas mixture [52] and lowering the voltage applied to the electrodes [53]. Due to this advantage, avalanche mode RPCs are mainly chosen for a high particle rates environment, like the muon trigger systems of the ATLAS [54] and CMS experiments at CERN [55].

Because the average pulse charges are ten times lower than in streamer mode, the avalanche mode allows this device to operate at a larger particle rate, up to a few kHz/cm2 [56] because it reduces the dead time of the detector. But this low pulse makes it necessary to amplify the readout signal, and so low noise electronics are needed.

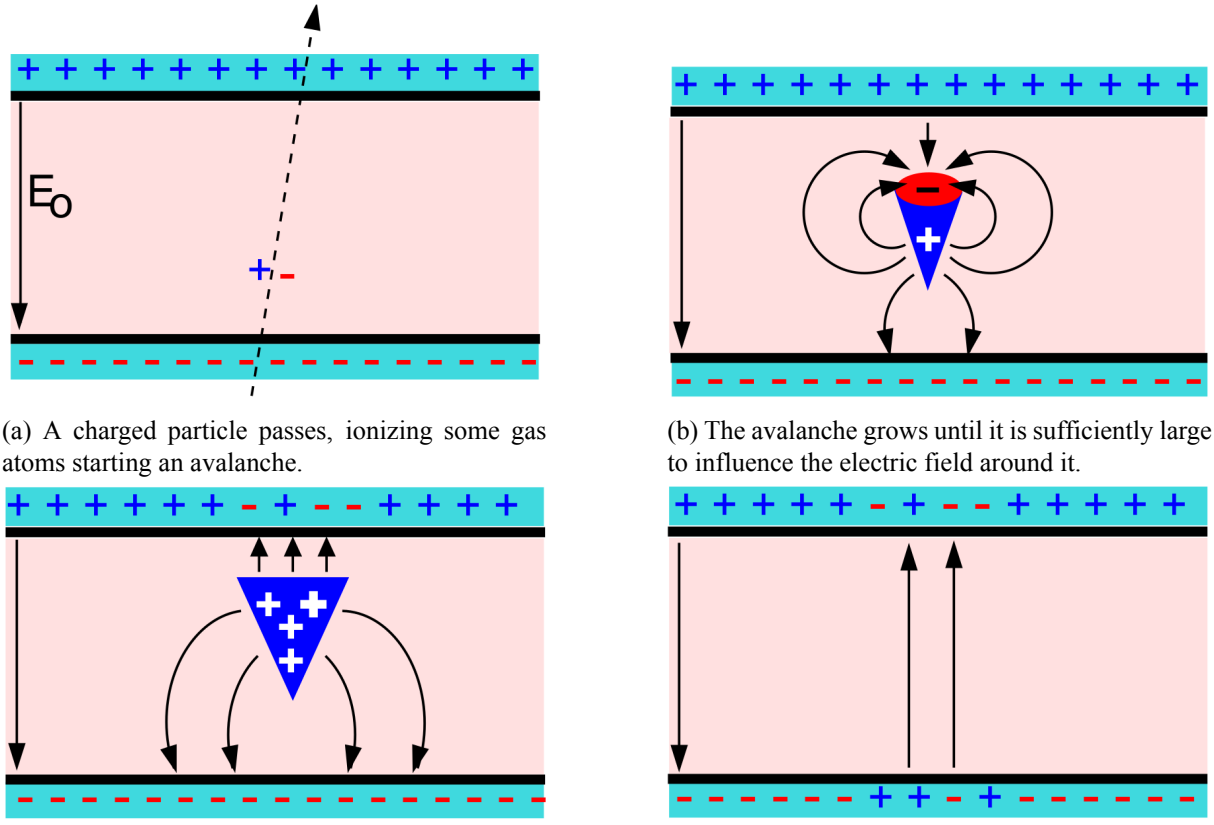

(a) A charged particle passes, ionizing some gas atoms starting an avalanche.

(b) The avalanche grows until it is sufficiently large to influence the electric field around it.

(c) The electrons reach the anode before the ions reach the cathode, because of the difference in drift velocities.

(d) The ions reach the anode. The charges in the resistive layers influence the field in a small area around the position where the avalanche developed.

Figure 3.2: A schematic view of the formation of an avalanche inside of a one-layer RPC. [42]

If the gas gain is further increased, photons start to contribute to the propagation of the avalanche, forming streamers [53]. At later stages, streamer development might create a conductive channel between

the electrodes, resulting in a localized discharge of the electrode surfaces and potentially a weak spark. See Figure 3.3 for the schematic view of the formation of a stream.

While streamer formation is unwanted in avalanche mode RPCs, it becomes the underlying principle for streamer mode operation. Streamer mode RPCs exploit the large current pulses generated by streamers, simplifying the readout process by providing a stronger signal while compromising the high rate capability.

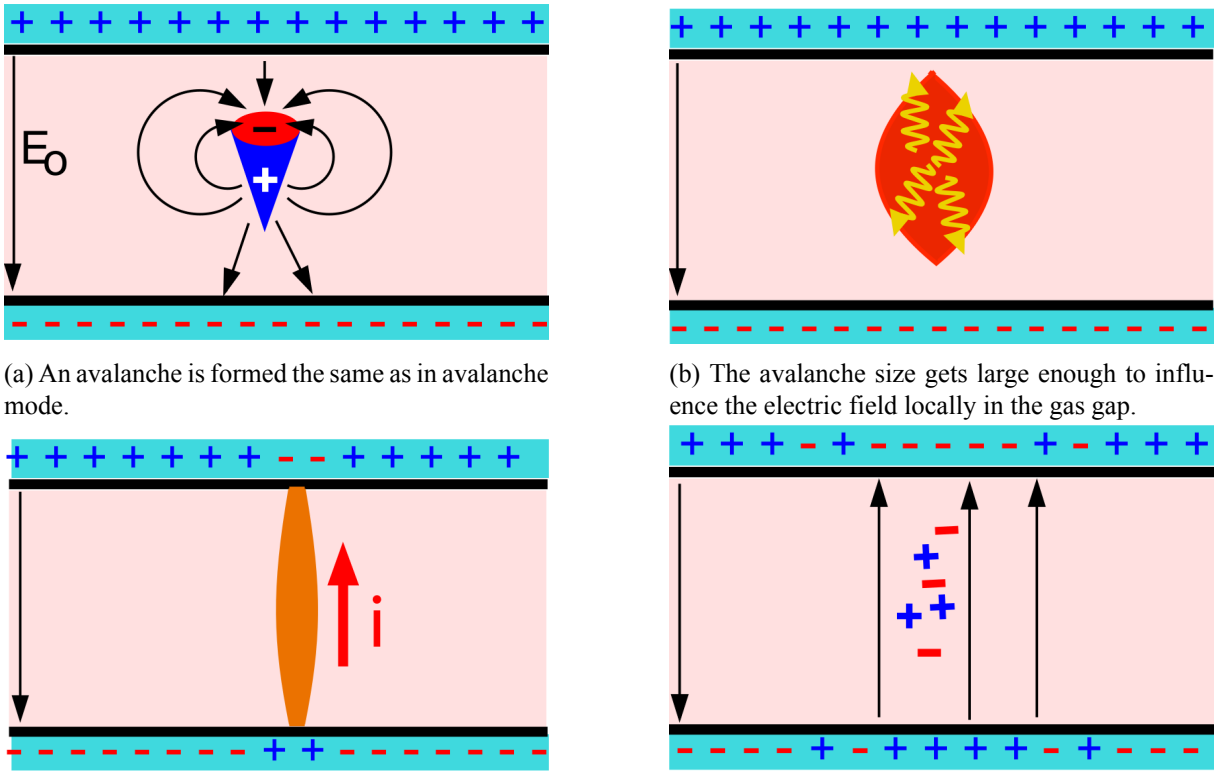

(a) An avalanche is formed the same as in avalanche mode.

(b) The avalanche size gets large enough to influence the electric field locally in the gas gap.

(c) The electrons reach the cathode (positive). The ions drift much slower to the anode (negative).

(d) The ions reach the cathode. The charges in the resistive layers influence the field in a small area around the position where the avalanche developed.

Figure 3.3: A schematic view of the formation of a stream inside of a one-layer RPC. [42]

Types of RPCs

There exist two different designs of RPCs: the *Trigger RPC* and the *Timing RPC*. While the distinction is not entirely clear, timing RPCs typically have much better time resolution compared to trigger RPCs. So the former detectors are typically used for Time-Of-Flight (TOF) measurements in many experiments while Trigger RPCs are typically used to detect the passage of Minimum Ionising Particles (MIPs) such as muons and signaling the other co-detectors and their data acquisition systems to record the data.

3.4 Resistive Plate Chamber at R3B

The RPC in R^3B is a multi-gap RPC with twelve layers. The twelve layers are separated in two modules, each of them with six gas gaps (98% $C_2H_2F_4$ and 2% SF_6) in open loop, defined by seven $1\,\mathrm{mm}$ thick float glass electrodes, with a bulk resistivity of $\approx 4 \times 10^{12}$ Ωcm at $25\,^{o}\mathrm{C}$, of about 1550×1250 mm², giving the RPC an area of almost $2\,\mathrm{m}^2$. These are separated by $0.3\,\mathrm{mm}$ nylon mono-filaments. These modules are confined in a permanently sealed plastic gas-tight box equipped with feed-throughs for gas and High Voltage (HV) connections. The electrodes comprise a semi-conductive layer applied to the outer surface of the outermost glasses.

The readout strip plane is equipped with forty-one copper strips ($29\,\mathrm{mm}$ width, $30\,\mathrm{mm}$ pitch, and $1600\,\mathrm{mm}$ long) located in between the two modules. The strips are read from both sides by a fast Front End Electronics (FEE) [57] capable of encoding in a single output signal the time (leading edge), with precision $<30\,\mathrm{ps}$ and charge (pulse width), which is lower than the precision the RPC can provide, so it does not affect the resolution. There are also two ground planes, located on top and bottom of the two-module stack. The whole structure is enclosed in an aluminum box for electromagnetic insulation and mechanical rigidity. See Figure 3.4 for a schematic view of this RPC [12].

This RPC, Figure 3.6, can achieve a time resolution down to $50\,\mathrm{ps}$ and efficiencies above 98% for minimum ionizing particles. It first was introduced as part of the setup of the FAIR Phase-0 experiment that focused on measuring for the first time, nucleon-nucleon short-range correlations (SRC) inside an exotic nucleus (16C). Since then has been part of other experiments and will be in future ones as well. Table 3.1 summarizes the experiments this RPC was part of at GSI.

Table 3.1: List of past and future experiments that the RPC present at R^3B was and will be part of.

Experiment Code	Experiment Title	Spokesperson	Year
S522	First characterization of Short-Range Correlations in exotic nuclei	Anna Corsi	2022
S509	Study of multi-neutron correlations in drip-line nuclei.	Olivier Sorlin	2022
S118	R^3B - 2023 Commission	Roman Gernhaeuser	2024
S091	Probing nucleon correlations in atomic nuclei via (p,pd) QFS reactions	Marina Petri	2024
S073	Matter radius of the hyperhalo candidate 3ΛH from interaction cross-section measurements	Alexander Oberteli	2025

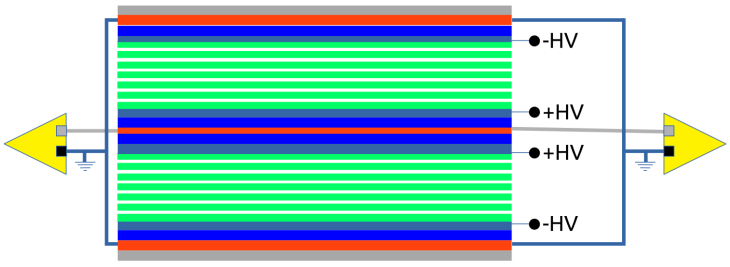

Figure 3.4: Schematic view of the RPC installed at R3B. It consists of 12 layers composed of glass and gas. It is separated into two parts of 6 layers. Gray — Aluminum box. Red — Readout electrodes. Blue — Plastic tight box. Black — HV electrodes. Green-Glass Electrodes. Yellow triangles — FEE. [12].

3.5 Simulations - R3BRoot

Before any experiment, running computer simulations is a necessary first step. These simulations are a critical tool for analysing and predicting complex physical systems and processes over time. They utilize computer models that encapsulate the fundamental physical laws governing these systems. However, the simulations are never an exact copy of real-life conditions and involve making necessary simplifications and approximations to, balance accuracy with computational efficiency and usability.

R3BRoot [58] is the framework used at FAIR for data analysis and simulations. It is built upon the FairRoot [59] tasks and Geant4 [60]. These frameworks also serve as the base library classes for many other experiments at FAIR. Some aspects that the FairRoot base library provides are:

- Common data structure for simulation and analysis based on Root Trees;
- Common geometry description based on the Root Geometry Modeler;
- Interface to different Monte Carlo engines using the Root Virtual Monte Carlo package [61];
- Detectors base class handling initialization, geometry construction, hit processing (stepping action), and others;
- Geometry input readers supporting Ascii, Root, and STEP (CAD) formats;
- Generic event display based on Eve and Geant;

R3BRoot builds upon this and provides additional classes for R^3B. These classes contain several tools like:

- Detectors geometry and materials;
- Magnetic field maps;
- Detectors hit registration;
- Dedicated physics list for low energy neutrons and gamma interactions and nuclear fragment transport;
- Dedicated event generators;
- Database connectivity to handle multiple experimental setups;

R3BRoot has the great advantage of providing the same tools and data structures for both simulation and experimental data, this way comparing results from experiments and simulations becomes more straightforward.

Figure 3.5 shows an example of a simulation environment in R3BRoot, where several detectors of the R3B experiment can be seen. This whole simulation is modular, meaning that each detector can be removed without affecting the rest of the simulation. This shows the versatility and robustness of this simulation tool.

The module of the RPC is shown in Figure 3.6a. It is comprised of the 12 gas layers discussed before, alongside it, in Figure 3.6b, is a picture of the real RPC placed after the GLAD magnet.

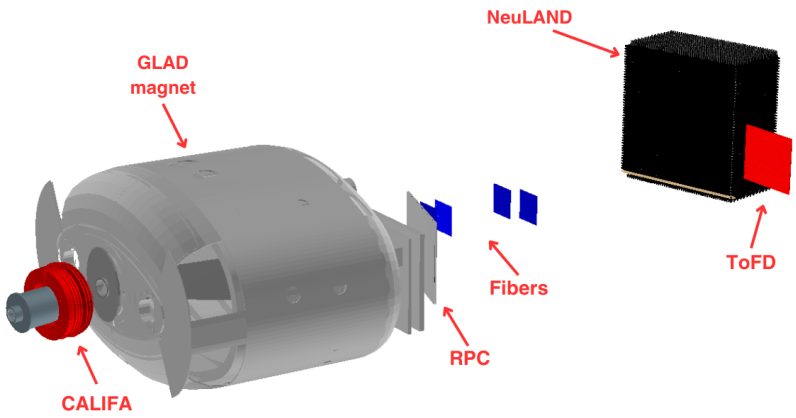

Figure 3.5: Example of an R3BRoot simulation. Several systems can be observed: CALIFA (surrounding the target), GLAD, the RPC, fibers, ToFD, and NeuLAND.

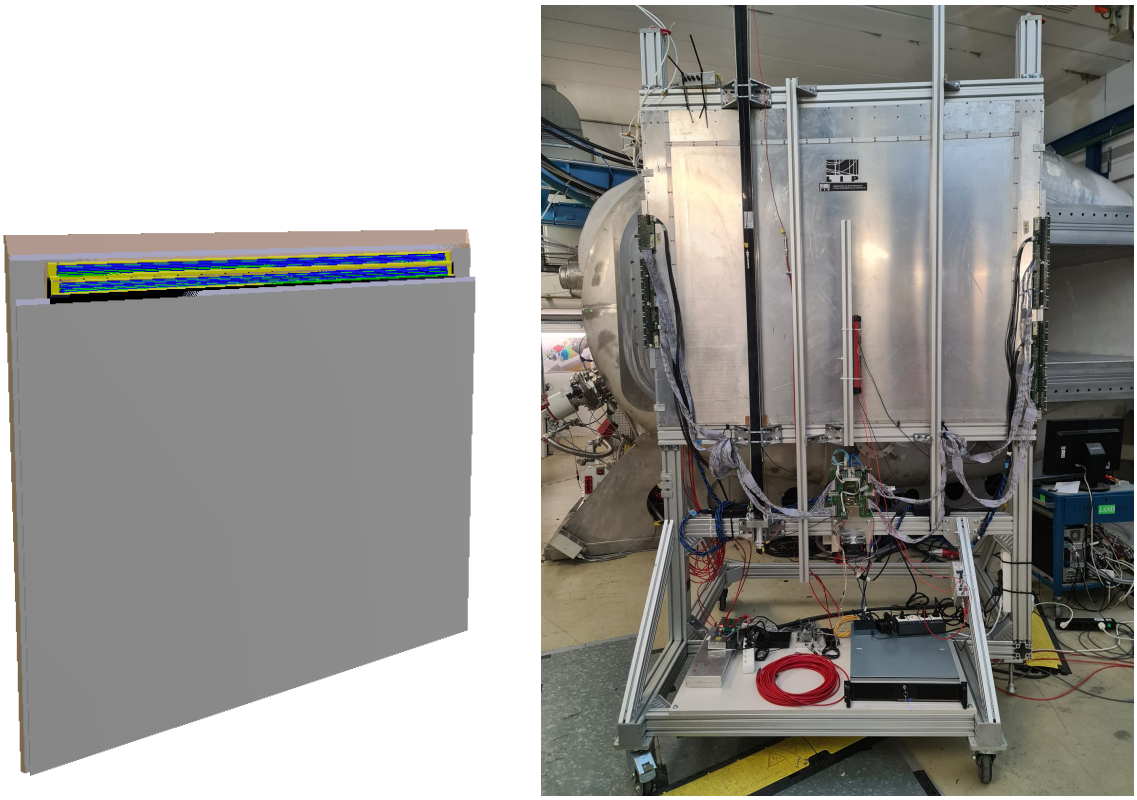

(a) Example of an R3BRoot simulation.

(b) RPC at R3B setup.

Figure 3.6: (a) RPC in R3BRoot simulation environment. (b) RPC at R3B setup.

Chapter 4

Momentum determination with the system CALIFA + RPC

This chapter discusses the results of the simulation studies performed on the proposed RPC concept working together with CALIFA and the corresponding data analysis.

To benchmark this novel detector concept, the particles selected in this study were **protons**, **deuterons**, and **alphas**. These particles were chosen as they are the most commonly produced light-charged particles in R^3B experiments, which, due to their high energies, punch through CALIFA reaching the space where the new RPC is proposed to be located. Each particle type was simulated at three different energy levels: 400, 500, and 700 $\mathrm{MeV/u}$. This set of simulations serves as a base for exploration of the performance of the RPC detector under different particle types and energies.

All simulations were performed using one particle per event and with a total of 5000 events, to ensure enough statistics while maintaining a reasonable simulation time. The RPC is positioned behind CALIFA, at the coordinates (50, 0, 90) in centimeters in the coordinate axis of the simulation environment, where the (0,0,0) point is the target position, as shown in Figure 4.1. This corresponds to a distance of 103 cm from the target to the center of the RPC. The RPC model used consisted of twelve layers of glass and gas. This configuration also accounts for the presence of aluminum plates, PMMA plates, and copper strips. The model does not consider the CALIFA mechanical structure nor the electronics associated with the readout signal from each crystal. To account for the possible contribution of these elements to the final momentum resolution, in Section 4.3, an additional homogeneous silicon block with 10 cm was added between CALIFA and the RPC, placed on the surface of the latter. This was a first step to investigate the effect of dead material in the setup. This large amount of silicon simulates the possible upper limit value obtained in this system. In reality, the non-homogeneity of the dead material will possibly lead to slightly larger uncertainties, but not to larger momentum shifts. This precise investigation is beyond the scope of this work.

The results from the simulations, in which different data branches contained the variables recorded for each of the detection systems considered, was a ROOT file [62]. This file was used for post-processing and analysis of data.

4.1 Momentum Reconstruction

To reconstruct the momentum of the simulated particle, a dedicated code is utilized to sort through the simulated data, retrieving the **time** and **position** values of the RPC hits. These values are then used to calculate the velocity, necessary to obtain the relativistic Lorentz factor through equation 4.1:

$$\gamma = \frac{1}{\sqrt{1 - \left(\frac{v^2}{c^2}\right)}} \tag{4.1}$$

This is then used to obtain the value of the momentum, through equation 4.2. This is done for each event and a histogram is created and filled with the momentum value.

$$P = mv\gamma \tag{4.2}$$

The simulations are only comprised of one particle per event. But, as the digitizer of the RPC simulation in R3B presently does not include a routine to analyze multiple hits in the detector done by the same particle, in those cases, our analysis calculates the average of the position and time hits, ensuring for each event a more reliable simulation.

As mentioned before, the simulations were systematically performed considering an incremental evolution of its complexity, analyzing the detector's resolving power capabilities, and evaluating the impact of the different variables in the obtained particle momentum resolution. As the final momentum determined will be affected by the crossing of large blocks of material, the correlation of the energy deposited in CALIFA and the reconstructed momentum will be studied as well, proposing a method to calibrate and correctly reconstruct the momentum of the originally emitted particle.

4.2 Establishing the Impact of CALIFA

To investigate the effect of the pure detector material of CALIFA in the determination of the particle momentum, two setups were studied. Initially, the system consisted of only two components: the GLAD magnet and the RPC, as presented in Figure 4.1a. This minimal configuration aimed at setting a baseline understanding of how the RPC would behave. The second setup introduced the bare crystals of the CALIFA detector alongside GLAD and the RPC, Figure 4.1b. This second setup aims to evaluate how the presence of CALIFA affects the reconstruction of the momentum.

Figure 4.2 shows the reconstructed momentum of a proton particle with an energy of $500\,\mathrm{MeV/u}$, equivalent to a proton with momentum equal to $1095\,\mathrm{MeV/c}$. The two peaks represent the considered setups with CALIFA (blue histogram) and without (red histogram).

This result shows that the reconstruction of momentum closely aligns with the input in the setup without CALIFA, where the momentum has a mean value (μ) of $1094.5\,\mathrm{MeV/c}$ and a standard deviation (σ) of 8.0×10^{-3} MeV/c. As for the setup with CALIFA, the mean value is $973.8\,\mathrm{MeV/c}$ with a standard deviation of $9.0\,\mathrm{MeV/c}$, an offset of $121\,\mathrm{MeV/c}$ compared to the nominal value. This effect is not surprising as the energy lost by the nuclei in CALIFA results in an increase in the time needed to reach the RPC. But, more important than the mean value, is the standard deviation, since the offset can be

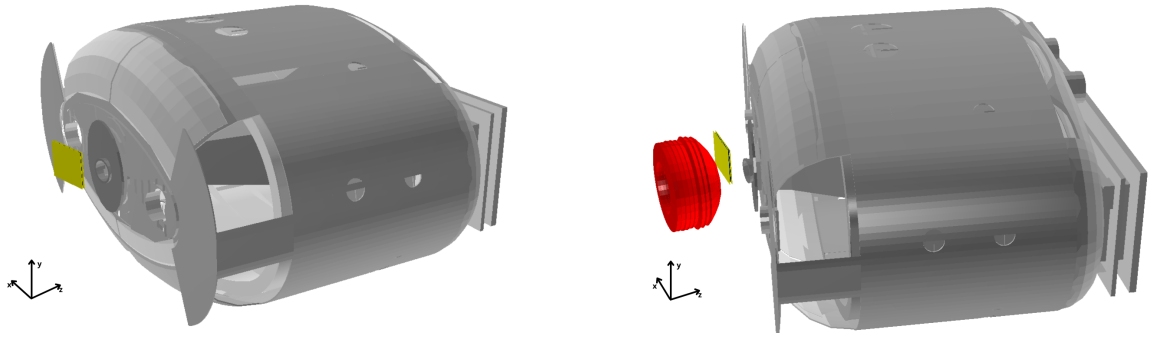

(a) (b)

Figure 4.1: Graphical representation of the simulation in the eventViewer of R3BRoot. The elements present in the images are the RPC in yellow; GLAD in grey; and CALIFA in red.

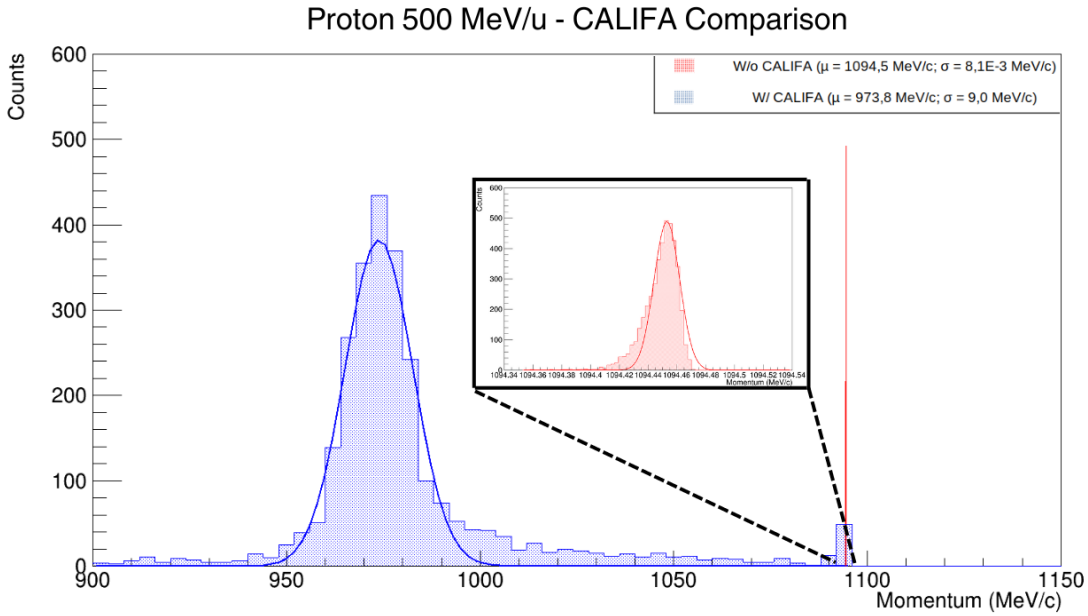

Figure 4.2: Momentum reconstruction of a proton with $p_0 = 1095\,\mathrm{MeV/c}$, corresponding to a proton with $E = 500\,\mathrm{MeV/u}$. In red, is the reconstructed momentum in the setup without CALIFA, and in blue is the setup with CALIFA.

corrected, but can only be trusted if the peak is well defined. The values obtained give us an uncertainty of $7.3 \times 10^{-3}\%$ for the setup without CALIFA and 0.92% for the setup where CALIFA is present, lower than the design value for CALIFA of 1%. Similar studies were performed for various particles and energies. In Figure 4.3 are plotted the resolutions of the three particles for all three energies. A general decrease in the resolution is seen throughout all particles as the energies are increased, with protons having the highest values, while deuterons have the lowest, below 0.5%. Alpha particles are in between, closely matching the proton values as the energy increases.

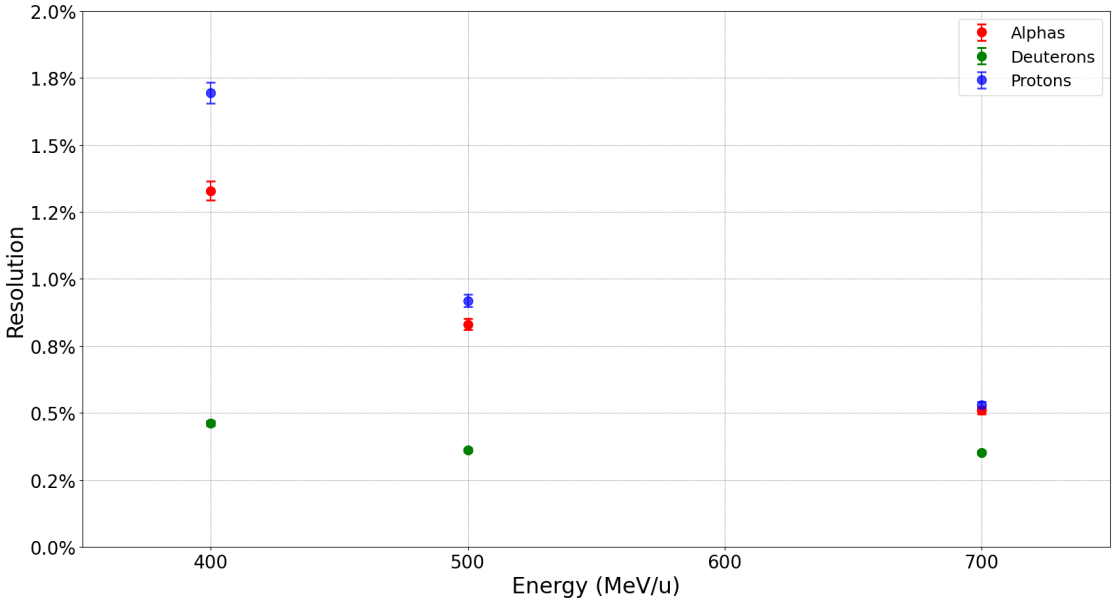

Figure 4.3: Momentum resolution as a function of the energy for the various particles considered in this work. The values correspond to the situation in which both CALIFA and RPC are present in the simulation.

The energy of incoming particles is frequently unknown in real-world situations. The value obtained in the RPC corresponds to the particle after it has traveled through CALIFA, where it loses some of its original momentum, resulting in a momentum offset. To correct this offset, we need to establish a link between the momentum offset and the energy deposited in CALIFA. With the type of particle detected and the energy lost in CALIFA known, we may adjust the observed momentum to obtain the proper value.

Figure 4.4 illustrates the offsets for the other particles at different energies, along with their respective errors. In general, the offsets decrease as energy increases for all particles, a pattern that is consistent with trends shown in Figure 2.4, where higher energy particles lose less energy when passing through the material, particularly for this energy region.

While the momentum offset for protons and deuterons is comparatively similar, alpha particles are approximately four times larger. This discrepancy comes from the amount of energy absorbed by CALIFA, an effect explained by the Bethe-Bloch Equation 2.9. Since the energies are per nucleon rather than the total energy of the particle, all particles have the similar velocities and beta values, for the same energy level. This makes the charge the biggest differentiator between them, appearing squared in the nominator of the Bethe-Bloch formula. Since alpha particles have double the atomic number of protons and deuterons, the energy lost is quadrupled, translating in the difference seen in momentum loss of alpha particles that arrive in the RPC.

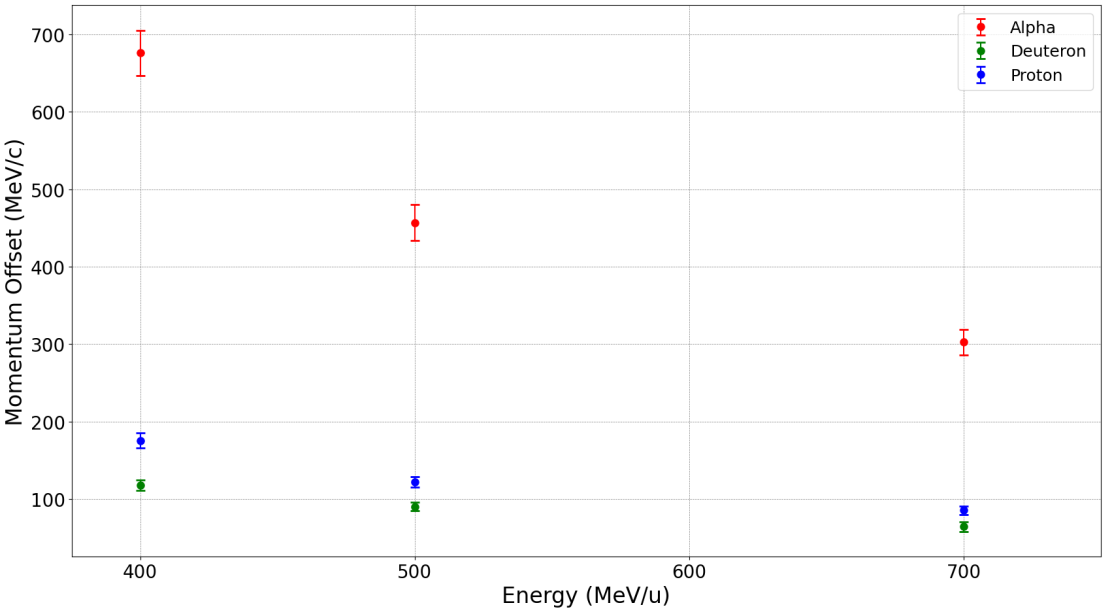

Figure 4.4: Offsets of momentum for the three particles and energies. Setup includes CALIFA.

The scatter plots for protons, deuterons, and alpha particles in Figure 4.5 depict the link between energy loss in CALIFA (MeV) and momentum offset (MeV/c). The three different clusters represent particles, and the three different energies are considered.

These figures show that, for all particle types, the momentum offset is reduced as the initial energy of the particle increases due to a decrease in energy loss in CALIFA. This regular pattern shows a strong association that can be utilized to ensure that particles passing through CALIFA have appropriate momentum reconstruction by correcting the momentum offset. For more details in these values see Table A.1 in appendix .

Peak Efficiency Estimation

As shown in Figure 4.6, the peak efficiencies are approximately 90% when the setup does not include CALIFA. However, when CALIFA is included, their efficiencies drop to 50%. The presence of CALIFA, with its 22 cm of crystal material, increases both the energy straggling and the probability of nuclear reactions for high-energy protons inside the crystals. These two effects lead to the observed efficiency drop.

These results points to a consistent pattern: the effect of CALIFA on the final momentum resolution is relativity small in an ideal situation where only the geometries of both the RPC and CALIFA are simulated. Furthermore, this action becomes less pronounced as the energy of the protons increases. Repetition of this analysis in subsequent simulations is rendered unnecessary by evaluating the behavior of the system in the absence of CALIFA. From now on, CALIFA will be included in all simulations.

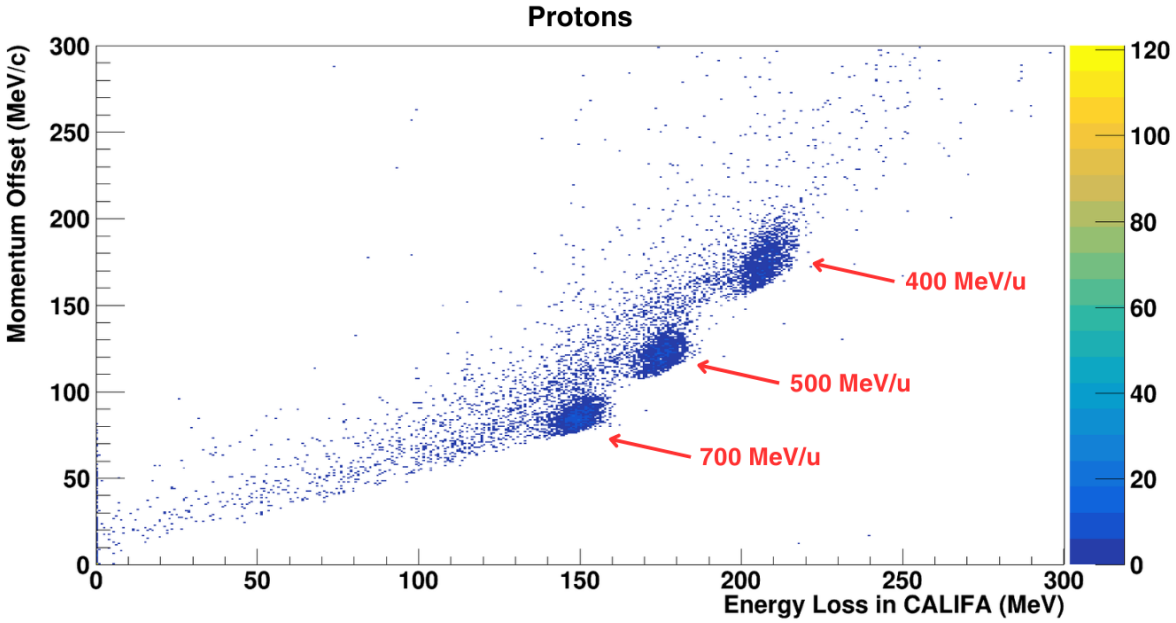
Protons
Momentum Offset (MeV/c)
Energy Loss in CALIFA (MeV)
400 MeV/u
500 MeV/u
700 MeV/u

(a)

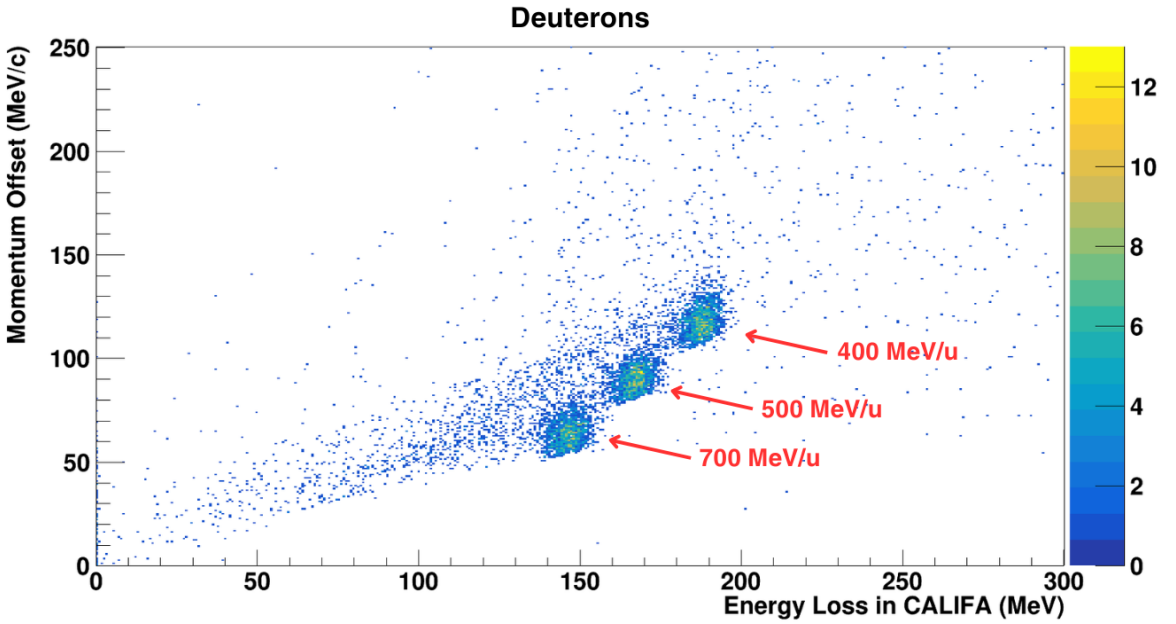
Deuterons
Momentum Offset (MeV/c)
Energy Loss in CALIFA (MeV)
400 MeV/u
500 MeV/u
700 MeV/u

(b)

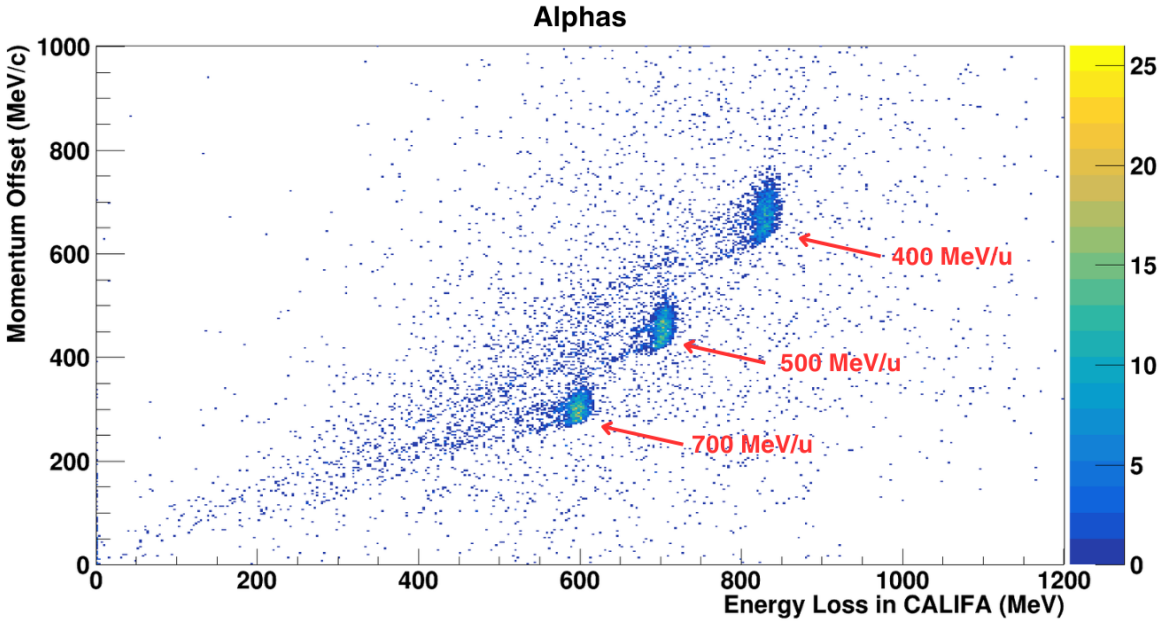

(c)

Figure 4.5: Scatter plots showing the momentum offset (MeV/c) versus energy loss in CALIFA (MeV) for all three particles. The clusters correspond to different energies of $400\,\mathrm{MeV/u}$, $500\,\mathrm{MeV/u}$, and $700\,\mathrm{MeV/u}$, as indicated by the red arrows.

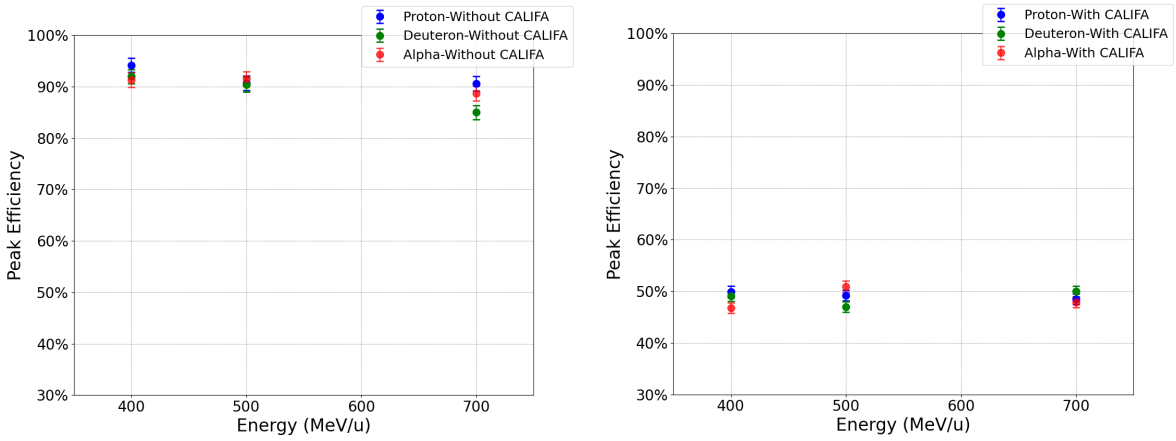

(a) (b)

Figure 4.6: Peak efficiencies for all three simulated particles and energies. Without CALIFA (a); With CALIFA (b).

4.3 Approaching structural elements: a Silicon Block

Until now, the simulation models used were considered ideal, simulating only the materials necessary for the basic operation of the detectors. This approach overlooked the mechanical structure and FEE electronics required for CALIFA, which are placed behind each crystal. Consequently, these will interfere with the flight path of the particles. As for the RPC, this is not a concern, because the electronics are placed around it, rather than in front, not interfering with the particle's flight path.

To have a rough estimate of the effect of these CALIFA components, the RPC geometry was modified as shown in Figure 4.7. This updated configuration retains the same 12 layers previously described while adding a compact block of silicon. This block acts as an obstacle in the flight path of the particles, with the purpose of replicating the electronics and support materials essential for the proper functioning of the CALIFA detector. The block is made of silicon for its density of $2.33\,\mathrm{g/cm^3}$, which closely matches the density of these electronic components.

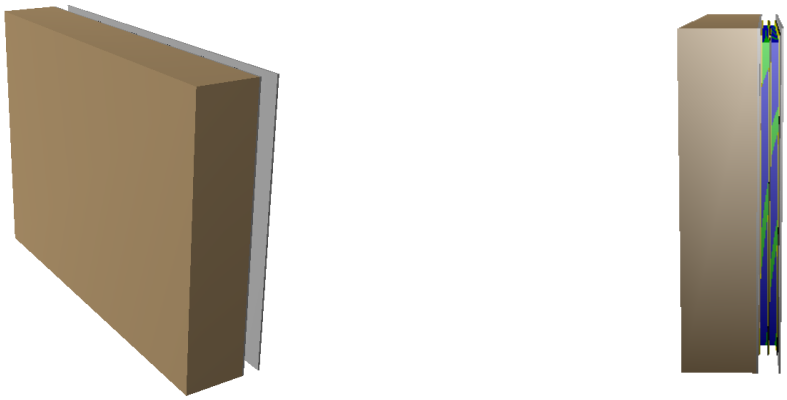

(a) (b)

Figure 4.7: RPC model in R3BRoot simulation, with the $10\,\mathrm{cm}$ silicon block in brown. Frontal and side view(a), side view (b).

As seen in Figure 4.8, tests were conducted on two distinct electronics thicknesses—$10\,\mathrm{cm}$ and $20\,\mathrm{cm}$—to investigate their impact on proton particles, even though it was anticipated that the electronics would be thinner than $10\,\mathrm{cm}$. With the $20\,\mathrm{cm}$ block, only 153 of the 5000 protons for $400\,\mathrm{MeV/u}$ protons (Figure 4.8a) reached the RPC, indicating a substantial attenuation for these particles. This means that applying this approach to lower energy particles is not feasible (efficiency of 3%). By comparison, the $10\,\mathrm{cm}$ block had an efficiency of 26.5% and made it easier for protons to reach the RPC.

It is also noteworthy that the impact of the thicker block is more significant for lower-energy protons. While the $400\,\mathrm{MeV/u}$ protons showed substantial attenuation, the $700\,\mathrm{MeV/u}$ protons achieved an efficiency of 43.8% with the $20\,\mathrm{cm}$ block. This difference is attributed to the fact that less energetic protons are more easily deflected within the material, drastically reducing the number that can reach the sensitive volume of the RPC.

These findings indicate that with a $20\,\mathrm{cm}$ block of silicon, the reliability of the data decreases significantly compared to the $10\,\mathrm{cm}$ block, making momentum reconstruction unpractical for low energies.

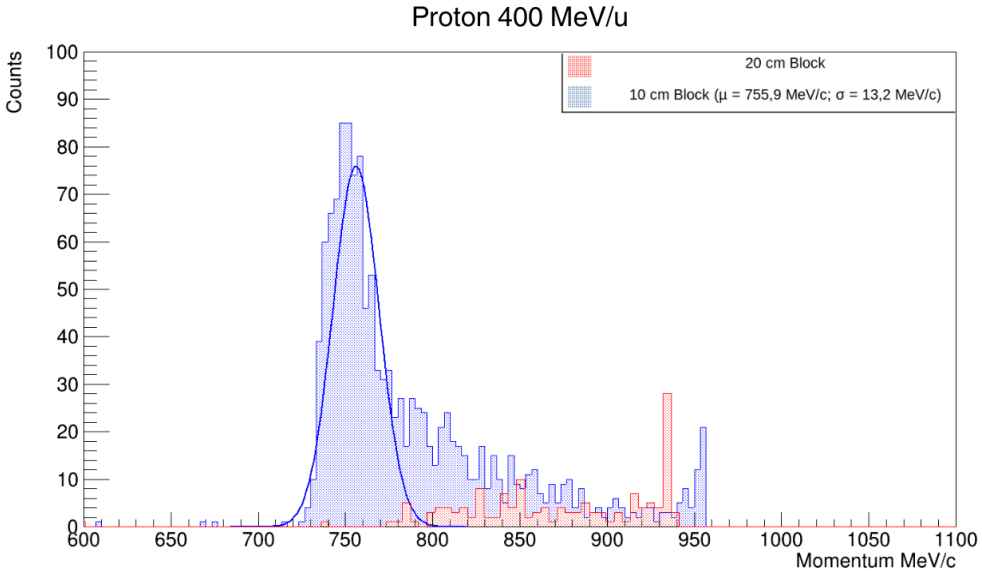

(a)

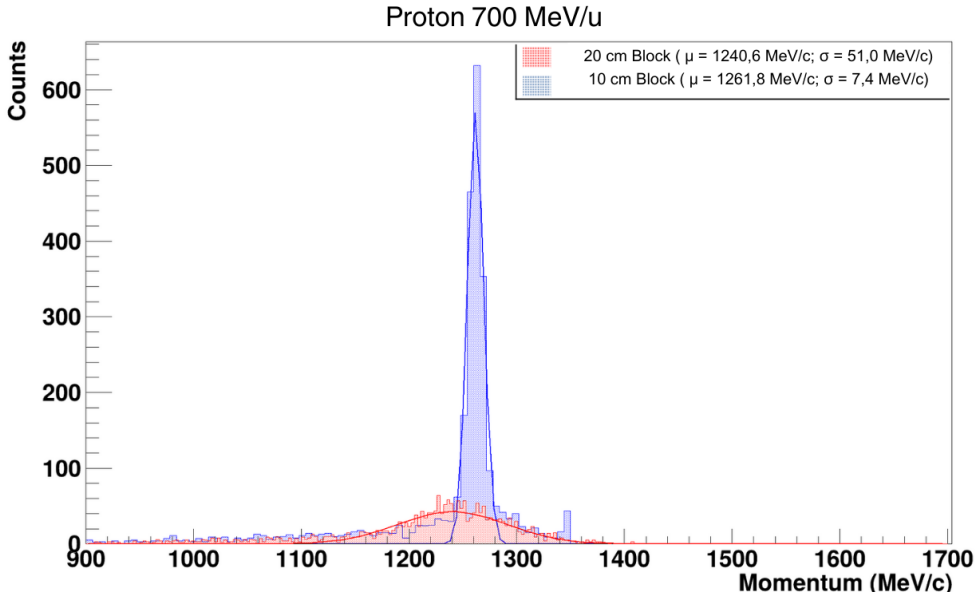

(b)

Figure 4.8: Comparison of proton simulations using a 10 cm silicon block (blue) and a 20 cm silicon block (red) at energies of 400 MeV/u (a) and 700 MeV/u (b).

Because the impact of the 20 cm block is less prominent on 700 MeV/u protons, it can still be effectively utilized for reconstructing the particle momentum with comparable uncertainty to the 10 cm scenario. Still, it is inferred that the material block should ideally not exceed 10 cm. Nonetheless, even in the 20 cm case, there are specific situations where data retrieval remains viable with a favorable level of uncertainty. To allow a comparison for various energies, the 10 cm block was considered for the rest

of the simulations.

We used the same protocol as before to assess how the silicon block affected the three particles. The change in reconstructed momentum for a $500\,\mathrm{MeV/u}$ proton after inserting the $10\,\mathrm{cm}$ block is shown in Figure 4.9a. The block-containing setup is displayed in blue in this figure, while the setup without the block is displayed in red. The most significant outcome is a change in momentum, where the particles lose $10\,\mathrm{MeV/c}$, which corresponds to $50\,\mathrm{keV/u}$ in energy. However, the peak resolution is not significantly affected, changing only from 0.9% to 1.2%.

Figure 4.9b illustrates that deuterons display a smaller change in momentum, $4\,\mathrm{MeV/c}$, which translates to an even smaller energy loss of $2\,\mathrm{keV/u}$. Similar to protons, the block's presence has little effect on the peak resolution (0.4%).

In the presence of the block, alpha particles experience an energy loss similar to protons, about $45\,\mathrm{keV/u}$, despite experiencing the largest momentum change, $36.5\,\mathrm{MeV/c}$. As seen in Figure 4.9c, the resolution with the block is 1%, whereas the resolution without the block is 0.8%.

Figure 4.10 illustrates these particles' detection efficiency. As shown in Figure 4.6b, the efficiencies are comparable to the arrangement without the block for energies of $500\,\mathrm{MeV/u}$ and $700\,\mathrm{MeV/u}$, particularly for alpha particles, nearing 50%. The efficiency of protons and deuterons is lower, approaching 40%. The lowest efficiency is 20%, seen for $400\,\mathrm{MeV/u}$ protons. This is directly related to the presence of additional material in the particles' flight path, which causes straggling and is more noticeable for lower energy and mass particles.

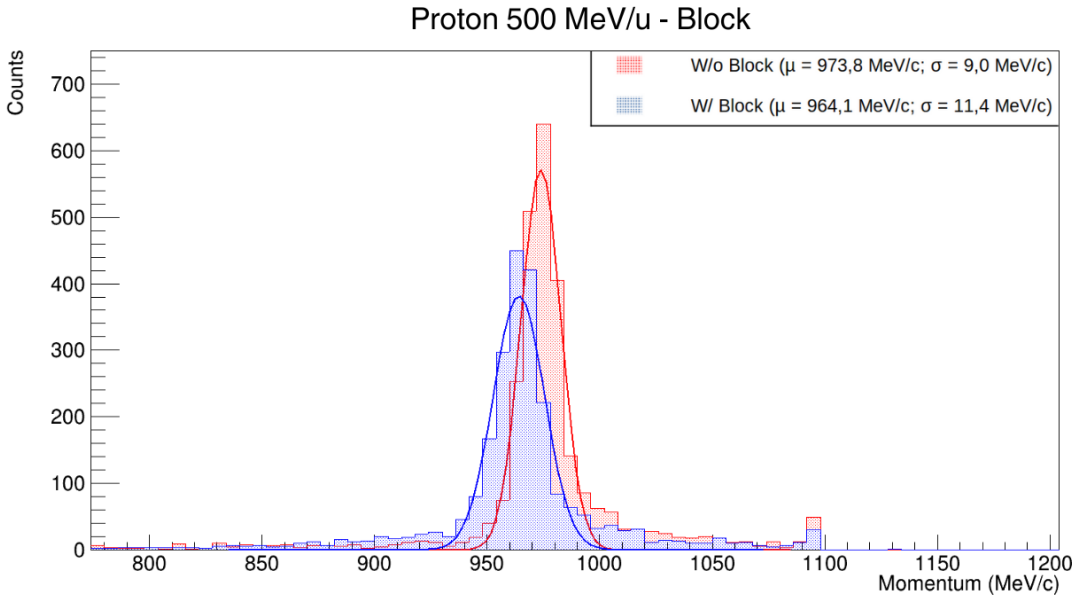

(a) $p_0 = 1095\,\mathrm{MeV/c}$.

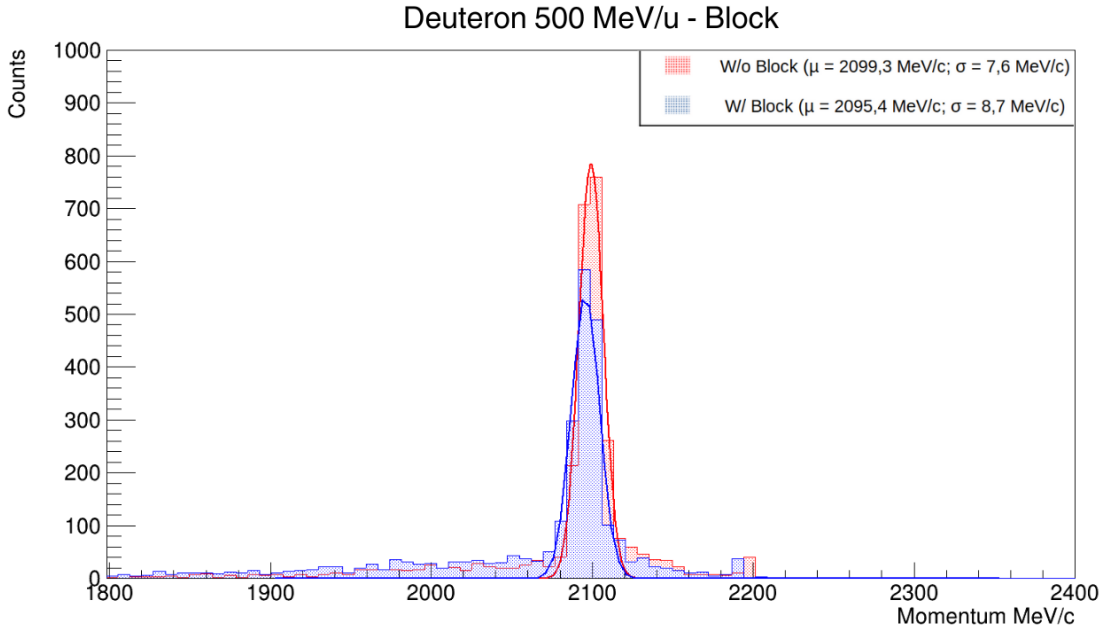

(b) $p_0 = 2189\,\mathrm{MeV/c}$.

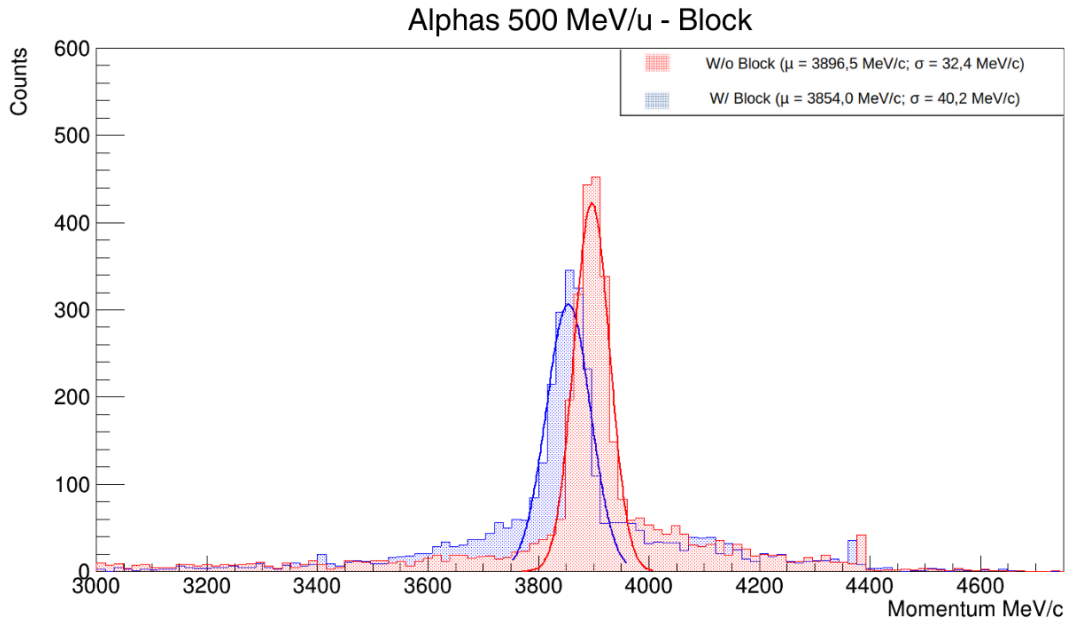

(c) $p_0 = 4349\,\mathrm{MeV/c}$.

Figure 4.9: Reconstruction of momentum of protons, deuterons, and alpha particles at $500\,\mathrm{MeV/u}$. This setup includes CALIFA and the $10\,\mathrm{cm}$ silicon Block.

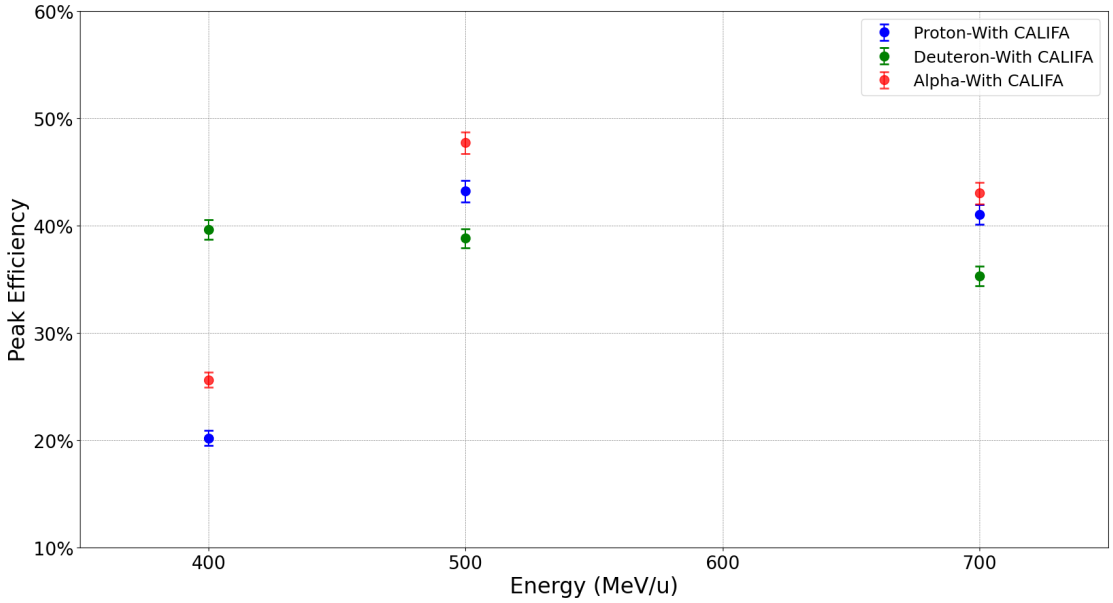

Figure 4.10: Peak efficiencies for all particles and energies. Setup with CALIFA and the 10 cm silicon block.

The 10 cm silicon block added to the experimental configuration has distinct effects on different particle types at 500 MeV/u. The presence of the block causes a small shift in momentum for protons and little effect on resolution, but nearly no changes for deuterons, indicating their resilience. On the other hand, alpha particles undergo substantial momentum shifts but the energy lost per nucleon is similar to protons. The 20 cm block is not suitable for such conditions since it results in significant attenuation, particularly for lower energy protons.

Overall, for protons, deuterons, and alpha particles, the 10 cm silicon block preserves dependable momentum reconstruction while introducing some energy loss and resolution degradation. Therefore, in simulations, it is best to use a 10 cm block to balance structural realism with data accuracy.

4.4 Studying the Impact of RPC Resolution

In previous simulations, the RPC was considered ideal and did not take into consideration its resolution limitations. To study the effect of the resolution of the RPC, four resolutions are now introduced in the code where momentum reconstruction is calculated, three for position and one for time.

To introduce these resolutions, a random number generator is used to generate values for each event hit and adds them to the nominal value of the variable in question. This deliberate introduction of jitters ensures that the reconstructed momentum aligns more closely with real-world scenarios, accounting for the inherent limitations of the detection system.

Random number generators follow specific statistical distributions. Gaussian distributions are used for the distribution of x, y, and time values. This choice was made because, even in situations where the precise distributions of the values involved are unknown, real-world random variables are generally

represented by the normal distribution. Equation 4.3 gives its probability density function.

$$f(x) = \frac{1}{\sqrt{2\pi\sigma^2}} e^{-\frac{(x-\mu)^2}{2\sigma^2}} \tag{4.3}$$

Here, μ is the mean of the distribution, and σ^2 is the variance. The standard deviation, σ is adjusted to emulate the real-world resolutions. The current RPC in the R^3B setup has a spatial resolution of $5\,\mathrm{mm}$, so the distribution for the x and y position values has a mean value of 0 and a standard deviation of $5\,\mathrm{mm}$. The time resolution is $50\,\mathrm{ps}$, and it is the value used for its distribution.

For the z direction, a uniform distribution is used. The probability density function is given in Equation 4.4. The values a and b for this distribution are -0.25 and 0.25, respectively. The uniform distribution is used for the z direction because the hit can occur anywhere with the same probability in this direction.

$$f(x) = \begin{cases} \frac{1}{b-a} & \text{for } a \leq x \leq b, \\ 0 & \text{for } x < a \text{ or } x > b. \end{cases} \tag{4.4}$$

To study the impact of the RPC resolution and how it affects the accuracy and reliability of the momentum reconstruction, a comparison is performed between the system with these resolutions added and without. Here the previous silicon block is removed to study the isolated effect of these resolution limitations. Figure 4.11 illustrates this comparisons for $500\,\mathrm{MeV/u}$ particles. In this figure, the perfect response configuration is shown in red, while the setup with the RPC resolutions is shown in blue.

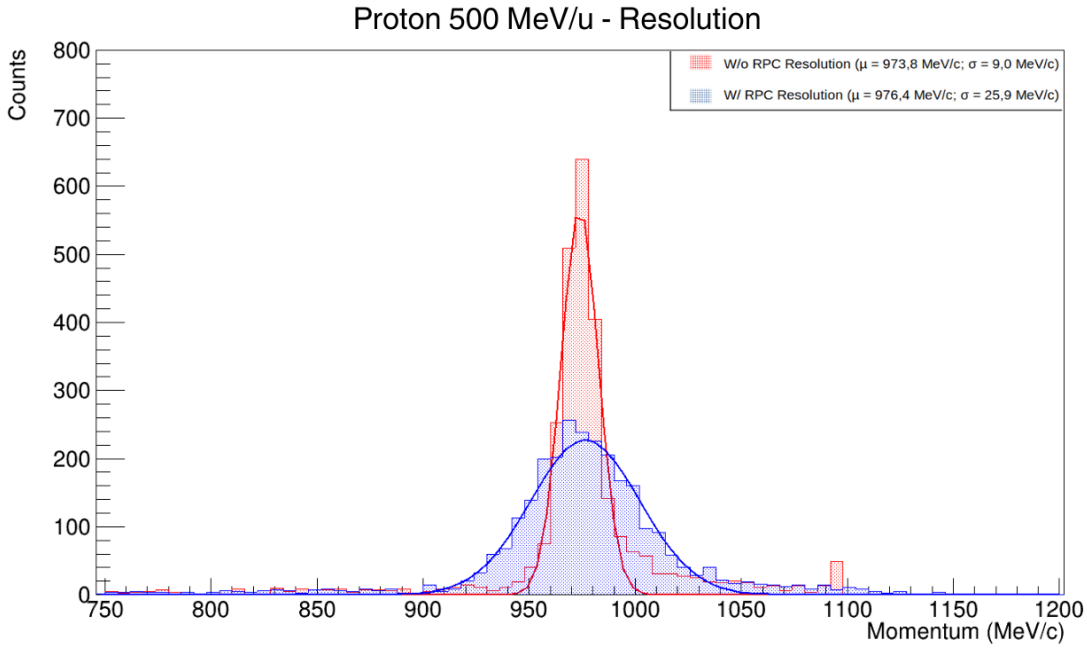

(a) $p_0 = 1095\,\mathrm{MeV/c}$.

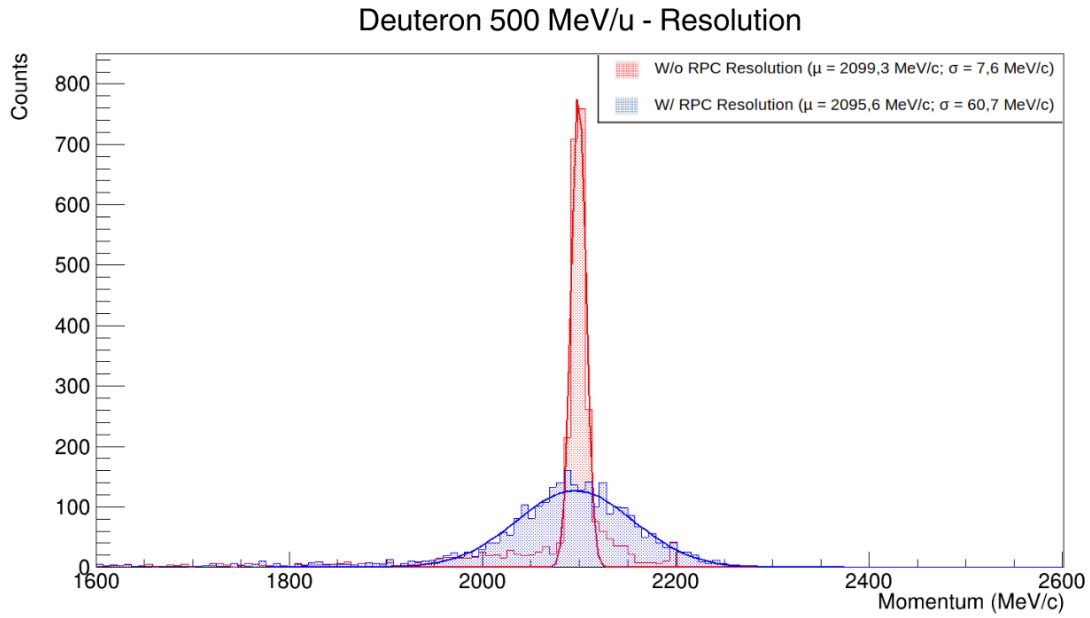

(b) $p_0 = 2189\,\mathrm{MeV/c}$.

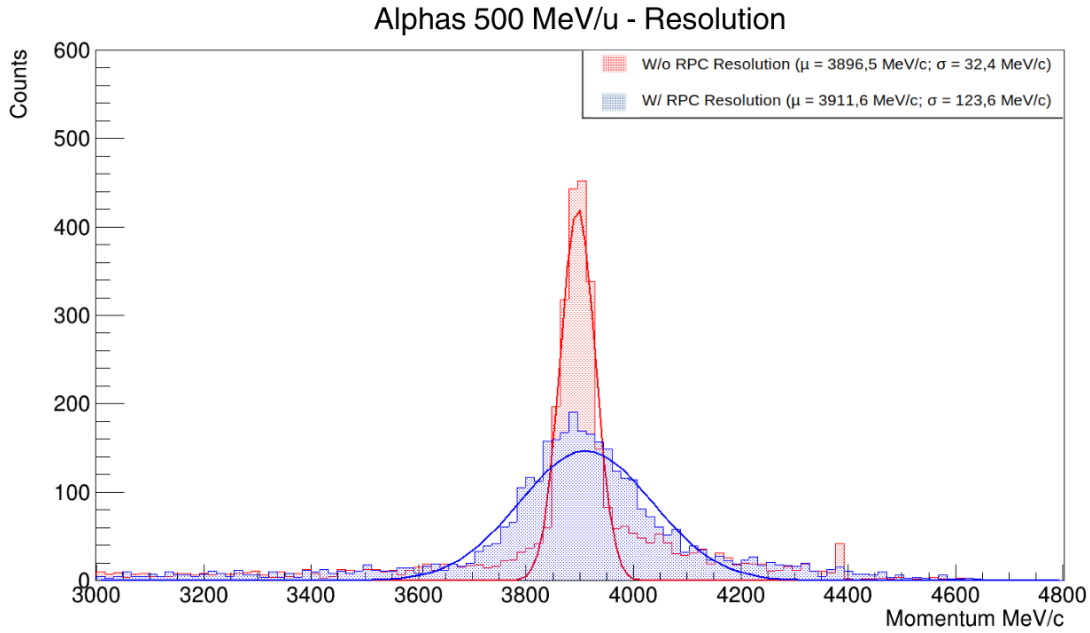

(c) $p_0 = 4349\,\mathrm{MeV/c}$.

Figure 4.11: Reconstruction of momentum for protons, deuterons, and alpha particles at $500\,\mathrm{MeV/u}$ energy. This setup includes CALIFA and the resolutions of the RPC.

The effect that is most notable by introducing the resolutions is that the reconstructed momentum is not consistently smaller than the ideal setup, unlike the silicon block setup. This happens because

limiting the detection capabilities of the RPC itself does not modify the mean value of the reconstructed momentum. Its primary impact is the increase of the standard deviation of the reconstructed momentum fits, resulting in less defined peaks. For protons, Figure 4.11a, the momentum resolution increases to 2.7%, a rise of 1.8% from the ideal setup. For deuterons, the resulting momentum resolution is about 2.9%, as shown in Figure 4.11b (0.9% in the ideal setup). In contrast to the optimal configuration where it is just 0.8%, the momentum resolution for alpha particles is 3.2%.

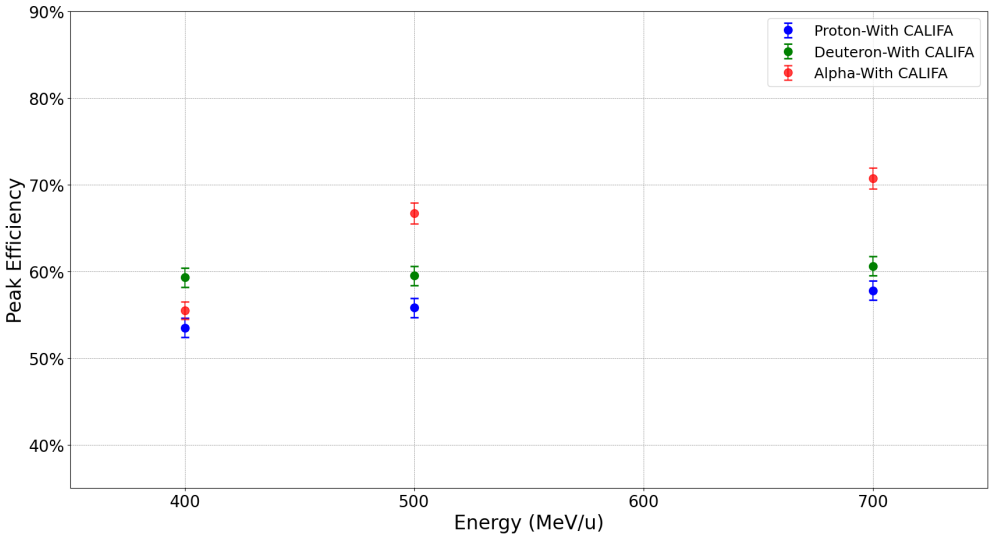

Figure 4.12: Peak efficiencies for all particles and energies. Setup with CALIFA and the resolutions of the RPC.

Figure 4.12 shows the peak efficiency for all particles at different energies when the resolutions are considered. Because there is nothing between CALIFA and the RPC to scatter or absorb the particles, the efficiencies are significantly higher than in the silicon block situation. Rather than changing the offset as the silicon block did, the primary impact of the jitters is an increase in the standard deviation in the fits of the reconstructed momentum, resulting in broader and less distinct peaks.

These results emphasize how important it is to consider the resolution limits of the RPC in simulations to gain a more accurate representation of detector performance in real life thereby enhancing the reliability and applicability of the simulation outcomes. Even though these resolutions are relativity worse, they are acceptable and better than the current setup at R^3B can offer.

4.5 The complete system: CALIFA + Silicon Block + RPC Resolution

To simulate real-world conditions as accurately as possible, the most comprehensive approach involves incorporating both the silicon block and resolution effects simultaneously. This simulation aims to account for both the physical interference of the FEE eletronics of CALIFA and the inherent limitations of any detector. By combining these two factors, a more realistic representation of the experimental setup and its impact on momentum reconstruction can be studied.

This simulation's output is shown in Figure 4.13. The reconstructed momentum for protons, deuterons, and alpha particles is shown in this picture, with the blue values signifying the combined effect of the silicon block and jitter on the detection and measurement procedures.

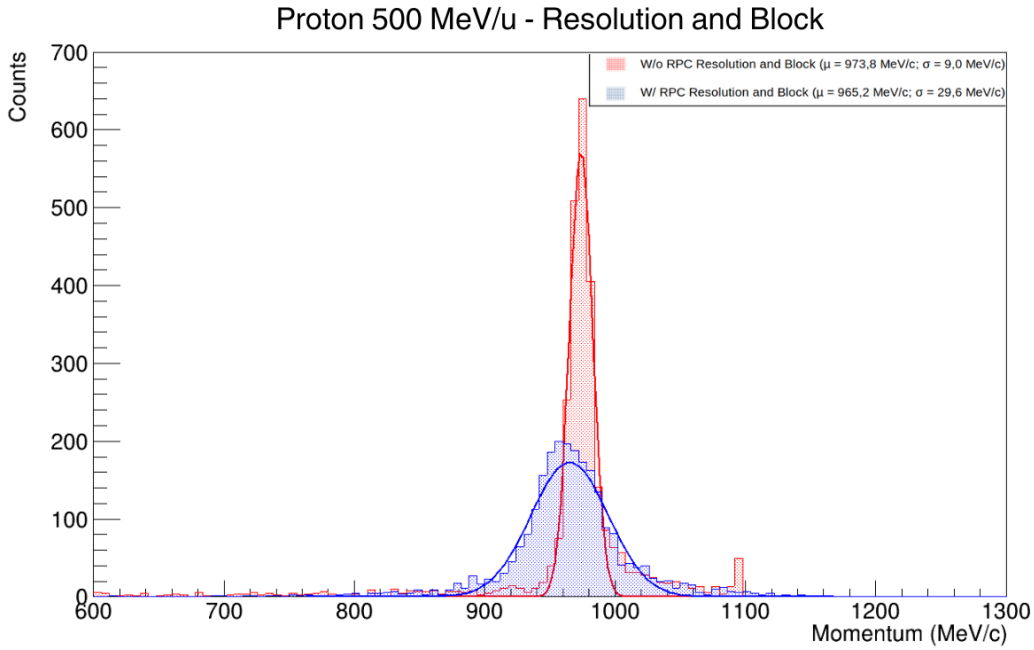

(a) $p_0 = 1095\,\mathrm{MeV/c}$.

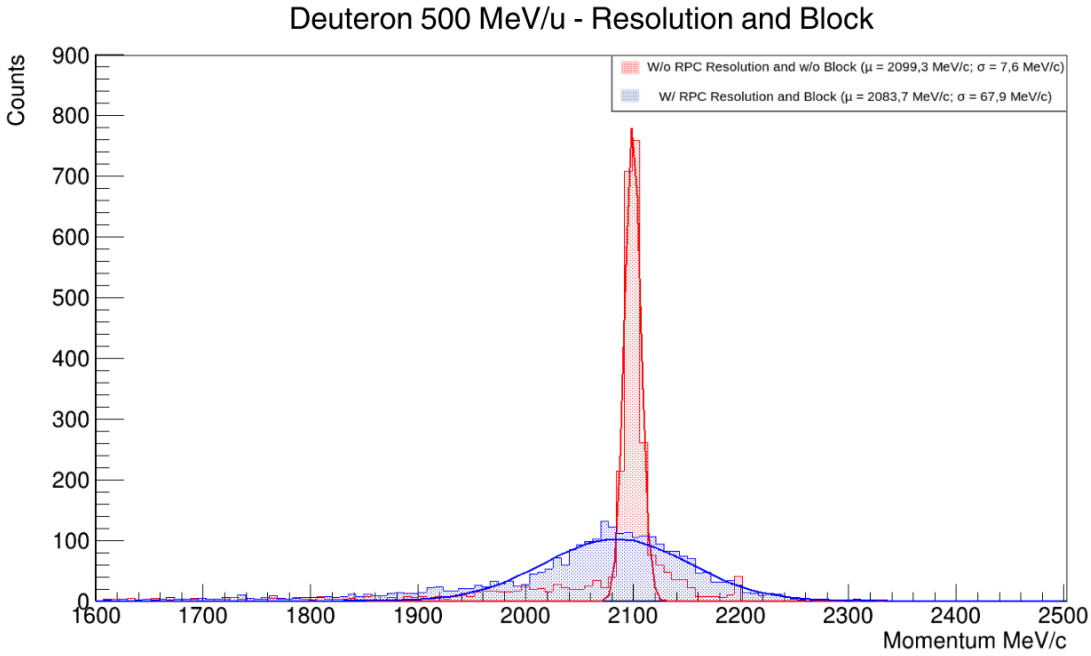

(b) $p_0 = 2189\,\mathrm{MeV/c}$.

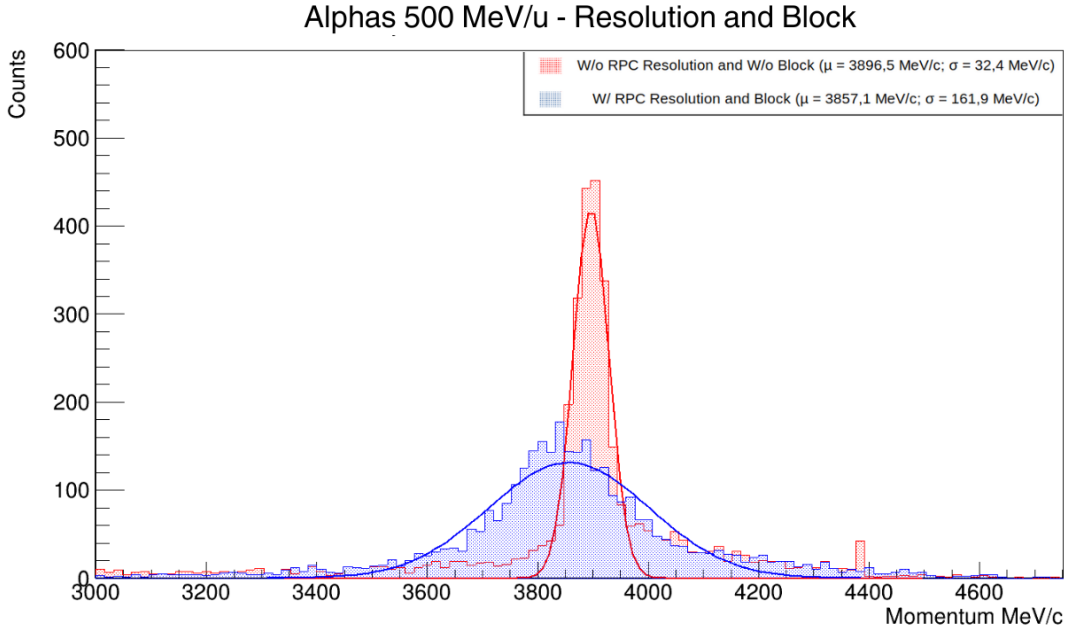

(c) $p_0 = 4349\,\mathrm{MeV/c}$.

Figure 4.13: Reconstruction of momentum for alpha particles at $500\,\mathrm{MeV/u}$ energy. This setup includes CALIFA, silicon Block, and RPC resolutions.

When both the resolutions and block are taken into account, the reconstructed momentum values for protons at $500\,\mathrm{MeV/u}$ are $965.2\,\mathrm{MeV/c}$ with a momentum resolution of 3.1%. The momentum resolution dramatically worsens with the addition of these elements, suggesting a major loss in measurement accuracy.

The reconstructed momentum value for deuterons at $500\,\mathrm{MeV/u}$ is $2083.7\,\mathrm{MeV/c}$ with a resolution of roughly 3.3%. Like protons, deuterons exhibit a significant increase in the width of the calculated momentum, which affects the precision of the measurement.

For alpha particles, the reconstructed momentum is $3857.1\,\mathrm{MeV/c}$ with 4.2% of resolution. Alpha particles exhibit the largest increase in the resolution value, reflecting the combined impact of the resolution and the silicon block on the precision of the momentum measurements.

Figure 4.14 illustrates the peak efficiencies for protons, deuterons, and alpha particles in a setup that includes CALIFA, a $10\,\mathrm{cm}$ silicon block, and the applied resolutions.

For protons, the efficiency starts at around 22% at $400\,\mathrm{MeV/u}$ and significantly improves to approximately 50% at both $500\,\mathrm{MeV/u}$ and $700\,\mathrm{MeV/u}$. This indicates that the presence of the silicon block and jitter does not drastically reduce the efficiency for protons at higher energies, suggesting that protons are less affected by these factors at $500\,\mathrm{MeV/u}$ and $700\,\mathrm{MeV/u}$.

Deuterons show a relatively high efficiency across all energy levels, starting at 51% for $400\,\mathrm{MeV/u}$ particles and reaching close to 55% at $500\,\mathrm{MeV/u}$ and $700\,\mathrm{MeV/u}$. This stability in efficiency indicates that deuterons are moderately affected by the silicon block and jitter, maintaining high efficiency across the energy range that was studied.

Alpha particles exhibit a similar trend compared to protons. At $400\,\mathrm{MeV/u}$, the efficiency is around 30%, but contrary to protons, it increases significantly to over 70% at $500\,\mathrm{MeV/u}$ and further to around 70% at $700\,\mathrm{MeV/u}$. This suggests that alpha particles are more resilient to the combined effects of the silicon block and jitter at higher energies, achieving better peak efficiencies.

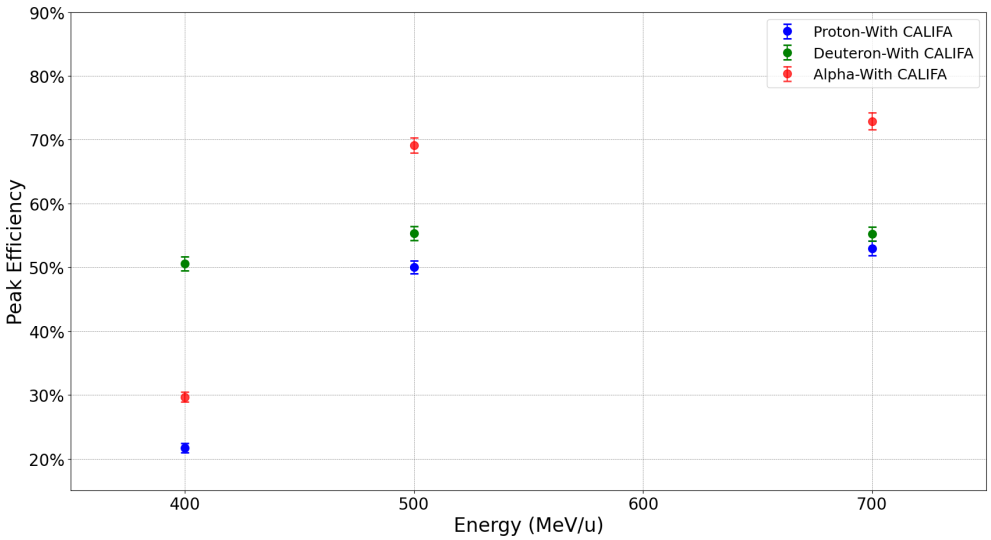

Figure 4.14: Peak efficiencies for all particles and energies. Setup with CALIFA, silicon Block and the resolutions applied.

4.5.1 Exploring the RPC Resolutions

In order to find out how the system reacts to different values of RPC resolution, it was performed a study using $500\,\mathrm{MeV/u}$ protons and several combinations for time and position resolutions. These results are shown in Figure 4.15. The position resolution in centimeters is represented in the x-axis in this heatmap, and the time resolution in picoseconds is represented in the y-axis. The percentage of momentum resolution is indicated by the color gradient and numerical values inside the cells. Values above 10% are not as desirable for the setup.

Practical limitations, however, must be considered. More specifically, because of technological constraints, present RPCs struggle to reach temporal resolutions lower than 50 picoseconds. Larger position resolution values are also better from a cost-production standpoint because they have fewer channels and, thus, fewer electronics, which results in lower manufacturing costs.

Observing the heatmap, we can see the ideal scenario providing a benchmark for comparison, where the resolutions are set to zero. This gives the best possible momentum resolution of 1.2%. However, since this ideal condition is impractical, we need to focus on the more feasible regions of the plot.

Focusing on the practical time resolution range (50 ps and above), we notice that the position resolution does not affect the momentum resolution as much as the time resolution. At a time resolution of 50 ps, increasing the position resolution from 0.0 cm to 5.0 cm results in a gradual increase in momentum resolution from approximately 3% to 6.3%. This indicates that, while a larger position resolution is more

cost-effective, it does come with a reasonably manageable trade-off in resolution accuracy.

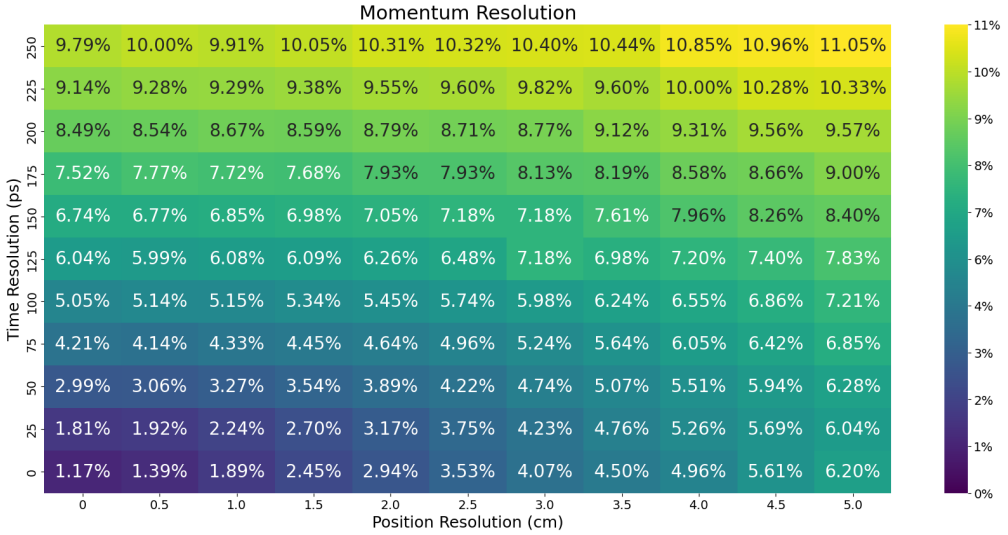

Figure 4.15: Comparison of momentum resolutions for protons particles at $500\,\mathrm{MeV/u}$, considering different values of position and time resolutions.

For time resolutions of 100 ps and 125 ps, the trend continues, with position resolution values up to 3 cm still maintaining a momentum resolution below 10%. Even lower position resolution values begin to provide resolutions that are close to 10%, making them less attractive, when the time resolution rises above 125 ps. For instance, even the $0.5\,\mathrm{cm}$ position resolution can not sustain the momentum resolution below 6% at $150\,\mathrm{ps}$ of time resolution.

According to this analysis, the time resolution should preferably be kept at 100 ps or less, and the position resolution values should not exceed 3.5 cm, to maintain a momentum resolution below 10%. Greater position resolution values can save expenses, however, this benefit must be weighed against the requirement to keep resolution values at an acceptable level.

Figure 4.16 shows a comparison of momentum resolutions for protons, deuterons, and alpha particles at $500\,\mathrm{MeV/u}$ under various position resolution conditions. This serves to verify if the pattern shown with the $500\,\mathrm{MeV/u}$ protons applies to different particles and energies, without doing the full range of resolution for all the possibilities. The time resolution in these location resolution charts is 50 picoseconds. In this case, increased position jitter also results in a rise in momentum resolution, however, the effect is not as strong as it is for time jitter. This finding supports the hypothesis that, although position jitter affects resolution, it is less dangerous and more controllable than time jitter. Therefore, larger position jitter values provide a practical option without significantly sacrificing measurement accuracy.

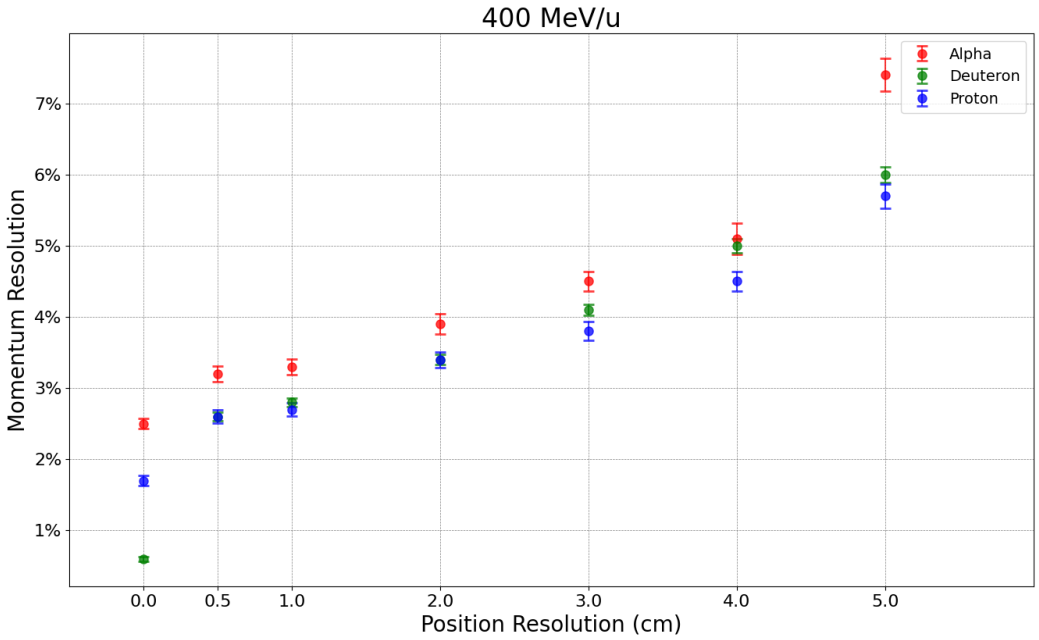
400 MeV/u
Alpha
Deuteron
Proton
Momentum Resolution
7%
6%
5%
4%
3%
2%
1%
0.0
0.5
1.0
2.0
3.0
4.0
5.0
Position Resolution (cm)

(a)

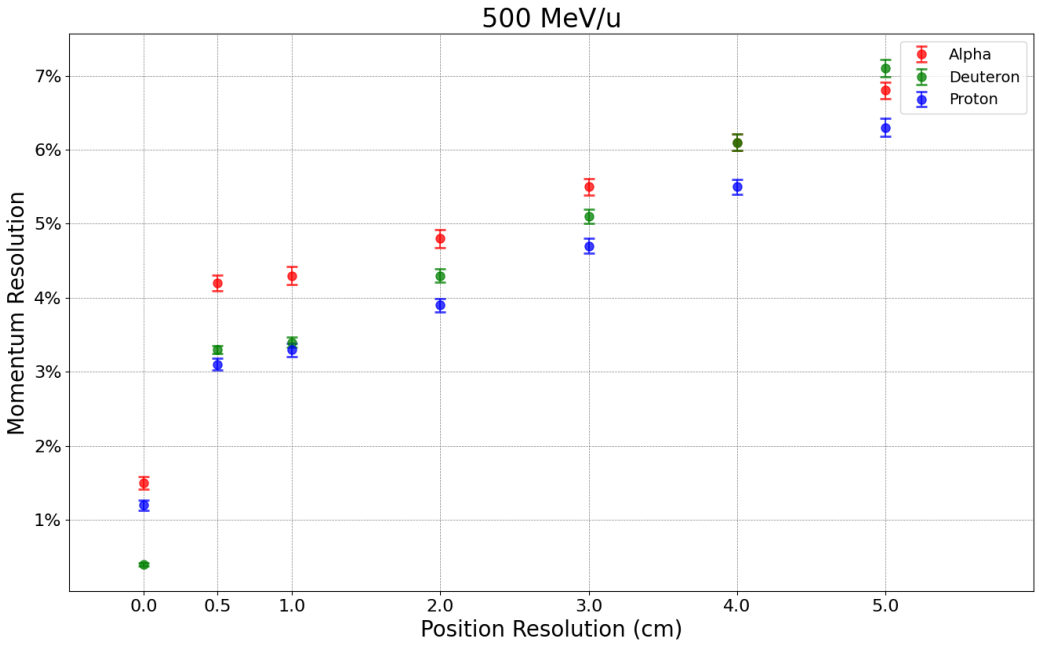
500 MeV/u
Alpha
Deuteron
Proton
Momentum Resolution
7%
6%
5%
4%
3%
2%
1%
0.0
0.5
1.0
2.0
3.0
4.0
5.0
Position Resolution (cm)

(b)

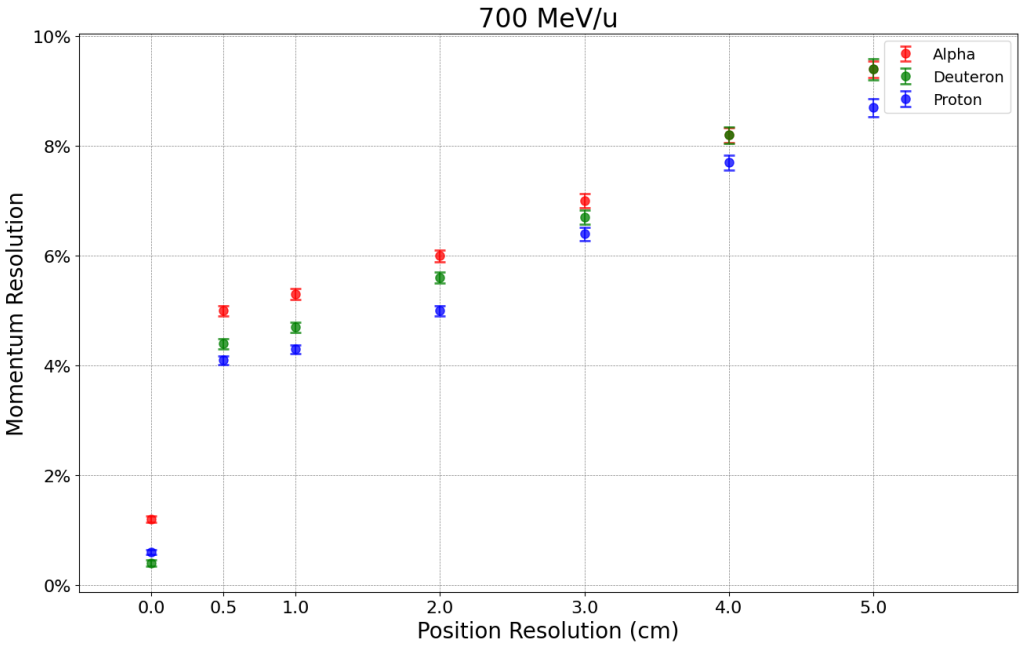

(c)

Figure 4.16: Momentum resolution as a function of position resolutions for protons, deuterons, and alpha particles.

In Figure 4.17, the focus is on time jitter, maintaining a position jitter of 0.5 cm. The result indicates that across all particle types, the momentum resolution gets worse as the time jitter increases. Notably, the dependence on time jitter is more significant than on position jitter. This finding is consistent with the heatmap analysis, where higher time jitters resulted in a more pronounced increase in momentum resolution.

From these plots, we can see that all particles follow similar trends, with protons exhibiting the lowest resolutions while alphas are the highest, but all within acceptable values.

These findings reveal the importance of prioritizing the reduction of the time resolution while allowing for some flexibility for the position resolution. By doing so, we can optimize detector performance, balancing cost and accuracy effectively. This analysis is necessary for the design and calibration of the RPC detector for this purpose, ensuring reliable and precise particle momentum measurements.

In summary, while the heatmap provides a detailed analysis for protons at $500\,\mathrm{MeV/u}$, the additional plots for various particle types and energies serve to validate the broader trends observed. The primary takeaway is that time resolution significantly impacts momentum resolution more than position resolution, making it critical to prioritize reducing time resolution while allowing for some flexibility in position resolution to balance cost and performance.

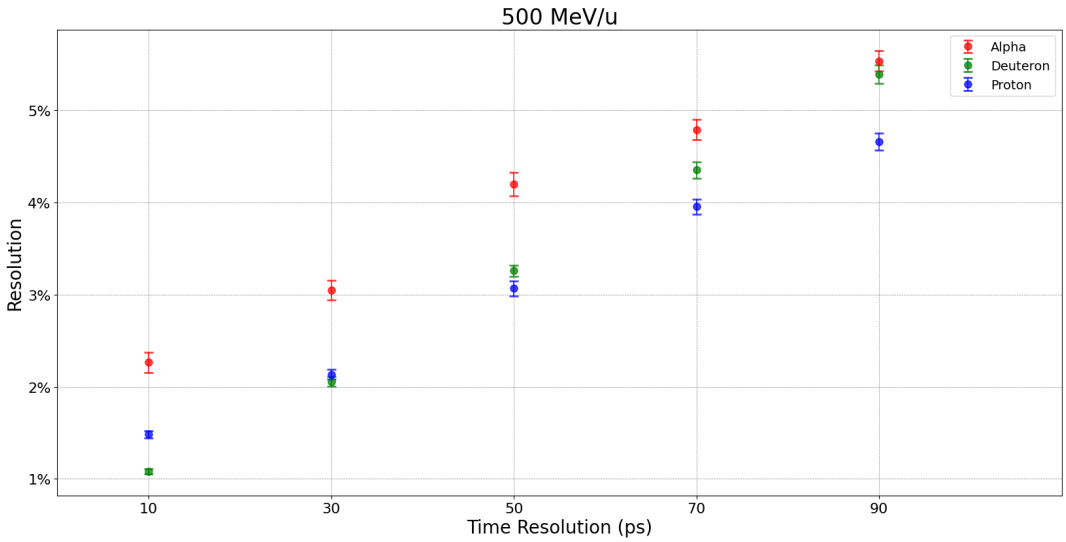

Figure 4.17: Momentum resolution as a function of time resolutions for protons, deuterons, and alpha particles.

Chapter 5

Benchmarking RPCs as an alternative for PAS

As mentioned in the introduction, after all contracts with the Russian Federation were interrupted in 2022, the R^3B PAS proposed concept had to be renewed, and as such the collaboration started a line of work in which both scintillating fibers and RPCs were considered as candidates for the construction of this branch of the R^3B experiment.

The alternatives tested for the Proton-Arm Spectrometer concept consisted of three different configurations. One where three fiber planes where used (Figure 5.1), another where one RPC is used in addition to the same three fiber planes (Figure 5.2a), and the last configuration used simply two RPCs (Figure 5.2b).

The mechanical and physical characteristics of these configurations were studied with MonteCarlo simulations within R3BRoot to see which of the concepts was able to reach the goals originally proposed in [31]. In this chapter, I present the results obtained for the concept of considering the RPC as a tracker system for forward-emitted relativistic protons.

In this setup, the two RPCs are separated by a distance of $1\,\mathrm{m}$. While the geometrical model used in these simulations is similar to the RPC currently installed at R^3B, the glass thickness is halved to 500 μm to minimize the material in the flight path of PAS. This reduction was implemented because, during the study of the fiber-only setup, it was shown that additional material negatively impacted the calculated momentum resolution for a position-based tracking algorithm. The RPC detector concept has not yet been benchmarked in a vacuum environment. Therefore, to investigate the effects of this limitation, simulations were done in three different ambient settings: Vacuum, Helium, and Air. Another aspect considered in these simulations was the effect of passive material at the entrance of GLAD. We then considered the Fiber23 detector concept, a scintillating tracking fiber system consisting of two planes of 300 μm fibers. Simulations with and without this detector were done and considered in the data analysis. These simulations consisted of 10^5 events, providing robust statistics for the MDF. Each event involves a single proton sent to enter GLAD where it deviates to the location of the proton branch detectors. For each setup, two energies were studied: $500\,\mathrm{MeV/u}$ and $1000\,\mathrm{MeV/u}$.

The momentum of the simulated protons was reconstructed using a Multi-Dimensional Fit (MDF) approach. A code developed by Valerii Panin and adapted to the RPC analysis by Manuel Xarepe for the

R^3B collaboration. The MDF was applied using two methods. The first method was position dependent, utilizing the entry position before GLAD and the final position at the first RPC, along with the angles derived from the pair of RPCs and the ToF between the proton source and the RPC detection point. The second method, the ToF-dependent, simplifies the calculations by not considering these angles, focusing solely on the ToF. In either case, the momentum resolution obtained for both tracking methods was calculated for various time and position resolution values of the RPC.

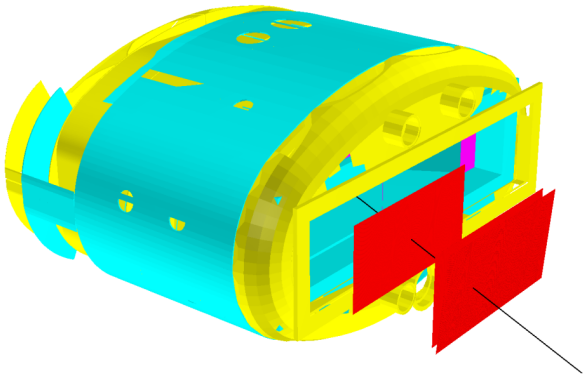

Figure 5.1: Setup for PAS concept with 3 fiber planes.

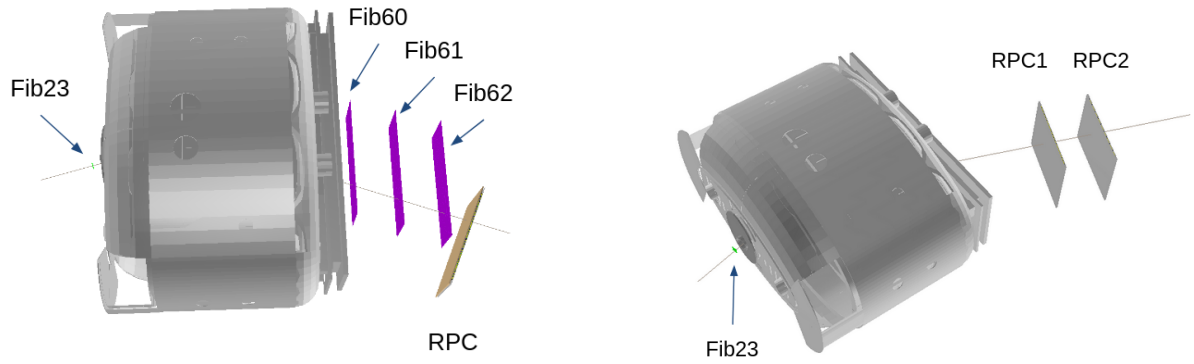

(a) (b)

Figure 5.2: Setups for PAS concept: (a) with fiber 23 behind GLAD, and fibers 60, 61, 62 and the RPC after GLAD; (b) with fiber 23 behind GLAD, and two RPCs after GLAD.

Figure 5.3 shows the uncertainty matrix for both the PD method and the ToF dependent method. In the PD MDF, the momentum resolution obtained for various RPC time and position resolution values considered is mostly constant, around 1.0% (one order of magnitude above the 0.1% momentum resolution goal). This effect strongly points out that the straggling in the RPC material dominates the resolution in the reconstruction using this PD MDF, and cannot be further improved. On the contrary, the ToF-dependent MDF yields better resolutions, around 0.5%, yet, still fails to meet the PAS design

goals. Additionally, the momentum resolution in the ToF-dependent MDF is rather independent of the position resolution, which aligns with the results obtained in the previous chapter, where the position resolution of the RPC does not affect the momentum resolution as much as the time resolution.

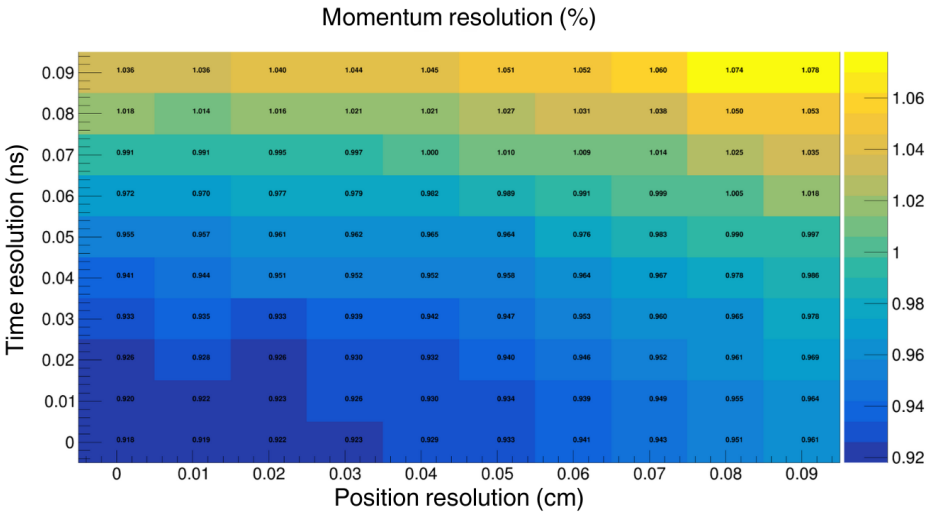

(a) Position-dependent MDF.

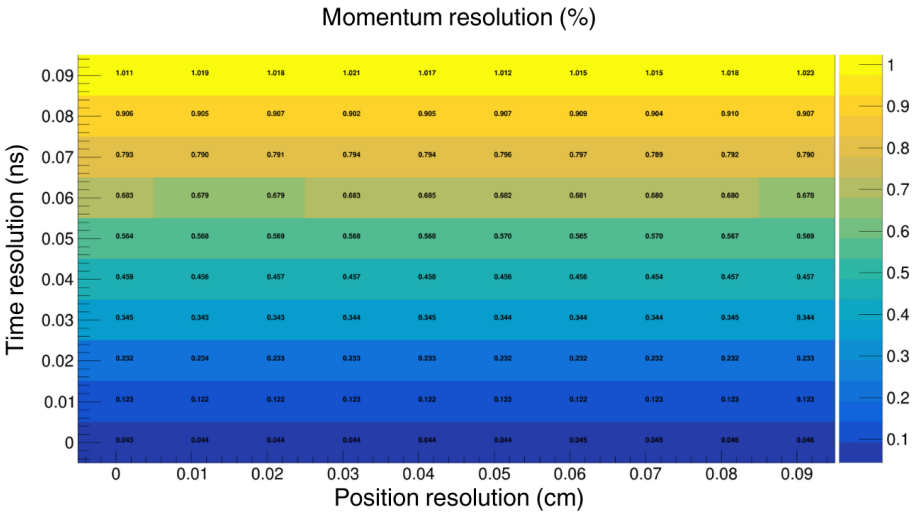

(b) ToF-dependent MDF.

Figure 5.3: Simulations with both RPCs in a vacuum: (a) Position-dependent MDF and (b) ToF-dependent MDF.

The momentum resolution results for different settings at position resolutions of 500 μm and time resolution of 60 ps are summarized in Table 5.1. When using helium as the medium, the momentum resolution closely matched that of the vacuum setting for both the position-dependent and TOF-dependent MDF methods. Specifically, the helium medium achieved a momentum resolution of 0.99% for the position-dependent MDF and 0.68% for the TOF-dependent MDF, which are identical to the results ob-

tained in a vacuum.

However, when air was used as the medium, the momentum resolution significantly deteriorated for the position-dependent MDF method. The results showed a resolution of 2.42% with Fiber 23 and 2.40% without it, indicating a notable degradation compared to the helium and vacuum settings. In contrast, the ToF-dependent MDF method was less affected by the change in medium, maintaining a resolution of 0.68% in air, which is consistent with the results in helium and vacuum.

The inclusion of Fiber 23 (X/Y) planes also had a minimal impact on the momentum resolution. Whether Fiber 23 was present or not, the resolution remained largely unchanged across different mediums.

These results highlight that while the medium plays a significant role in the position-dependent MDF method, it has a lesser impact on the TOF-dependent MDF method. Moreover, the presence of Fiber 23 does not significantly affect the momentum resolution in any of the tested scenarios. Another important aspect is that the ToF method, contrary to the position method and the fiber solution, is not affected by the quantity of material present, making it more robust for many experiments conducted at R^3B.

Table 5.1: Summary table of the data obtained in the implementation of RPCs for PAS.

(ΔX = ΔY = 500 µm & Δt = 60 ps)		**Fib23**	**Momentum Resolution (%)**
Position MDF	Air	YES	2.42
	Air	NO	2.40
	He	YES	0.99
	He	NO	0.99
	Vacuum	YES	0.99
	Vacuum	NO	–
ToF MDF	Air	YES	0.68
	Air	NO	0.68
	He	YES	0.68
	He	NO	0.68
	Vacuum	YES	0.68
	Vacuum	NO	–

Ultimately, as the design goals were not met in any of the configurations, the PAS concept using the RPC was not chosen, with the 3 plane fibers being the one selected. In table 5.2 is the summary of the most important results for PAS, with the fiber concept being very close to the original results from the straw-tube wall [63].

In any case, the work with RPCs provided valuable insights and comparisons that guided the eventual choice of the scintillating fiber-based design.

Table 5.2: Main PAS design criteria and obtained values for the Straw-Tube concept and for the Fiber PAS (measured using a prototype). Taken from [63].

Design criteria	Straw-Tube PAS	Fiber PAS
Position resolution σ_x	$200\,\mu\mathrm{m}$	$250\,\mu\mathrm{m}$
Angular resolution σ_Θ	$0.3\,\mathrm{mrad}$	$0.25\,\mathrm{mrad}$
MIP detection efficiency	$\geq 95\%$	$\geq 97\%$

Chapter 6

Conclusions

The proposal for this work was to explore the intricacies of designing and benchmarking the innovative concept of measuring light-charged particles with a Resistive Plate Chamber (RPC) detector placed behind CALIFA in the Reactions with Relativistic Radioactive Beams (R^3B) experiment. Effects produced by the inactive material in the flight path of the particles and how different spatial and temporal resolutions of the RPC affect the reconstruction of momentum were studied, offering significant insights for future optimization of an RPC in this application.

The comparison of momentum resolutions across protons, deuterons, and alpha particles at three energy levels – 400 MeV/u, 500 MeV/u, and 700 MeV/u – confirms that higher energy particles exhibit better momentum resolution. Protons generally display the best momentum resolutions, while alpha particles have the worst. This trend shows the importance of studying the detection system for specific particle types and energies for optimal performance.

The presence of CALIFA induced an offset in momentum values due to its active material, reducing the particle's energy by the time it reaches the RPC. However, this impact is lower as the energy of the particle increases, suggesting that higher energy particles deposited less of their energy to the material of CALIFA and suffered less energy straggling also affecting the peak efficiencies. The inclusion of CALIFA also reduced the detection efficiency due to the increased straggling. This effect is also less pronounced at higher energies, especially for protons.

The study of the resolution limits of the RPC reveals that both the resolutions of time and position significantly influence the final momentum resolution. Specifically, time resolution plays a more critical role than position. Maintaining a time resolution below $100\,\mathrm{ps}$ is crucial for achieving momentum resolutions under 10%, with the most preferable outcomes observed when the time resolution is below $50\,\mathrm{ps}$. Position resolution, although less critical, still has an impact on the final momentum resolution. The best results are observed when position resolution values do not exceed $3\,\mathrm{cm}$. As position resolution is not as critical as time resolution, it helps for a low cost-high benefit relation, which can guide the design to be more efficient.

The technological limitations in achieving very low time resolutions highlight the need for advances in detection electronics and materials. Future research should focus on modifying the properties of the RPC, like the number of gas gaps, their thickness, the glass plates thicknesses, and how they affect the detector's performance. These changes can result in a better resolution than the ones obtained by the RPC

model used in this study.

One of the alternatives for the straw-tube detectors in the Proton-Arm Spectrometer (PAS) concept, was two RPCs placed one meter apart and located behind the GLAD magnet. The RPCs model used had modifications such as halving the glass thickness to reduce material in the flight path which is critical in this application. Simulations were conducted in various environments – vacuum, helium, and air – and analyzed using a Multi-Dimensional Fit (MDF) approach for momentum reconstruction. The results revealed that the ToF-dependent MDF method consistently provided better momentum resolution, around 0.68%, across different media, and demonstrated robustness against material quantity, unlike the position-dependent method, significantly affected by the medium, particularly air. Despite the insights gained, the RPC-based PAS concept did not reach the tracking TDRTDR requirements and was ultimately not selected. Instead, the scintillating fiber-based design was chosen, closely aligning with the original straw-tube wall performance.

Implementing these findings in real-world experiments will require further study of the case and close collaboration with the R3B collaboration. The practical constraints and cost considerations discussed will play a crucial role in whether the idea is realized or not.

It is foreseen that the results from this work will be presented in future CALIFA working group meetings and to the R^3B collaboration.

References

[1] R3B Colaboration. https://www.gsi.de/work/forschung/nustarenna/nustarenna_divisions/kernreaktionen/activities/r3b. Accessed: March 06, 2024 (cit. on p. 1).

[2] T. Aumann et al. *Technical Proposal for the Design, Construction, Commissioning and Operation of R3B: A Universal Setup for Kinematical Complete Measurements of Reactions with Relativistic Radioactive Beams*. Tech. rep. GSI: R3B Collaboration, 2005. URL: https://www.gsi.de (cit. on pp. 1, 6).

[3] R3B Collaboration. *Technical Report for the Design, Construction and Commissioning of the Active Target for FAIR (ACTAF) for the R3B experiment*. Tech. rep. R3B Collaboration, Nov. 2016 (cit. on p. 1).

[4] Y. Aleksandrov, A. Zinevich, E. Leikin, et al. "A Liquid-Hydrogen Target". In: *Photomesic and Photonuclear Processes*. Ed. by D. V. Skobel'tsyn. Boston, MA: Springer US, 1967, pp. 185–190. ISBN: 978-1-4757-0139-5 (cit. on p. 1).

[5] H. Geissel, P. Armbruster, K.H. Behr, et al. "The GSI projectile fragment separator (FRS): a versatile magnetic system for relativistic heavy ions". In: *Nuclear Instruments and Methods in Physics Research Section B: Beam Interactions with Materials and Atoms* 70.1 (1992), pp. 286–297. ISSN: 0168-583X. DOI: https://doi.org/10.1016/0168-583X(92)95944-M. URL: https://www.sciencedirect.com/science/article/pii/0168583X9295944M (cit. on p. 1).

[6] H. Geissel, H. Weick, M. Winkler, et al. "The Super-FRS project at GSI". In: *Nuclear Instruments and Methods in Physics Research Section B: Beam Interactions with Materials and Atoms* 204 (2003). 14th International Conference on Electromagnetic Isotope Separators and Techniques Related to their Applications, pp. 71–85. ISSN: 0168-583X. DOI: https://doi.org/10.1016/S0168-583X(02)01893-1. URL: https://www.sciencedirect.com/science/article/pii/S0168583X02018931 (cit. on p. 1).

[7] R3B. https://edms.cern.ch/ui/file/1865815/2/TDR_R3B_TrackingDetectors_public.pdf. Accessed: March 07, 2024. 2023 (cit. on p. 1).

[8] B. Gastineau, A. Donati, Ducret, et al. "Design Status of the R3B-GLAD Magnet: Large Acceptance Superconducting Dipole With Active Shielding, Graded Coils, Large Forces and Indirect Cooling by Thermosiphon". In: *IEEE Transactions on Applied Superconductivity* 18.2 (2008), pp. 407–410. DOI: 10.1109/TASC.2008.922529 (cit. on p. 1).

[9] A. Macchiavelli M. Petri S. Paschalis. *Probing nucleon-nucleon correlations in atomic nuclei via (p,pd) QFS reactions*. Tech. rep. GSI, 2024 (cit. on p. 2).

[10] K. Boretzky, I. Gašparić, M. Heil, et al. “NeuLAND: The high-resolution neutron time-of-flight spectrometer for R3B at FAIR”. In: *Nuclear Instruments and Methods in Physics Research Section A: Accelerators, Spectrometers, Detectors and Associated Equipment* 1014 (2021), p. 165701. ISSN: 0168-9002. DOI: https://doi.org/10.1016/j.nima.2021.165701. URL: https://www.sciencedirect.com/science/article/pii/S0168900221006860 (cit. on p. 2).

[11] M. Heil, A. Kelic-Heil, L. Bott, et al. “A new Time-of-flight detector for the R3B setup”. In: *EUROPEAN PHYSICAL JOURNAL A* 58.12 (Dec. 2022). ISSN: 1434-6001. DOI: 10.1140/epja/s10050-022-00875-8 (cit. on p. 2).

[12] M. Xarepe, T. Aumann, A. Blanco, et al. “Resistive plate chambers for precise measurement of high-momentum protons in short range correlations at R3B”. In: *Nuclear Instruments and Methods in Physics Research Section A: Accelerators, Spectrometers, Detectors and Associated Equipment* 1055 (2023), p. 168445. ISSN: 0168-9002. DOI: https://doi.org/10.1016/j.nima.2023.168445. URL: https://www.sciencedirect.com/science/article/pii/S0168900223004357 (cit. on pp. 3, 24).

[13] R3B Collaboration. *Technical Report for the Design, Construction and Commissioning of The CALIFA Barrel: The R3B CALorimeter for In Flight detection of γ rays and high energy charged pArticles*. Tech. rep. R3B Collaboration, Nov. 2011. URL: https://wiki.r3b-nustar.de/_media/detectors/califa/califa_barrel_tdr_web.pdf (cit. on pp. 3, 5).

[14] R3B Collaboration. *Technical Report for the Design, Construction and Commissioning of the CALIFA Endcap*. Tech. rep. R3B Collaboration, Aug. 2015. URL: https://wiki.r3b-nustar.de/_media/detectors/califa/tdr_r3b_califa_endcap_public.pdf (cit. on pp. 3, 5).

[15] B. Pietras, M. Winkel, H. Alvarez-Pol, et al. “First testing of the CALIFA Barrel Demonstrator”. In: *Nuclear Instruments and Methods in Physics Research Section A: Accelerators, Spectrometers, Detectors and Associated Equipment* 814 (2016), pp. 56–65. ISSN: 0168-9002. DOI: https://doi.org/10.1016/j.nima.2016.01.032. URL: https://www.sciencedirect.com/science/article/pii/S0168900216000486 (cit. on p. 3).

[16] A. Knyazev, J. Park, P. Golubev, et al. “Properties of the CsI(Tl) detector elements of the CALIFA detector”. In: *Nuclear Instruments and Methods in Physics Research Section A: Accelerators, Spectrometers, Detectors and Associated Equipment* 940 (2019), pp. 393–404. ISSN: 0168-9002. DOI: https://doi.org/10.1016/j.nima.2019.06.045. URL: https://www.sciencedirect.com/science/article/pii/S0168900219308903 (cit. on p. 3).

[17] P. Cabanelas, D. González, H. Alvarez-Pol, et al. “Performance recovery of long CsI(Tl) scintillator crystals with APD-based readout”. In: *Nuclear Instruments and Methods in Physics Research Section A: Accelerators, Spectrometers, Detectors and Associated Equipment* 965 (2020), p. 163845. ISSN: 0168-9002. DOI: https://doi.org/10.1016/j.nima.2020.163845. URL: https://www.sciencedirect.com/science/article/pii/S0168900220303570 (cit. on p. 3).

[18] A. Knyazev, J. Park, P. Golubev, et al. “Tl concentration and its variation in a CsI(Tl) crystal for the CALIFA detector”. In: *Nuclear Instruments and Methods in Physics Research Section A: Accelerators, Spectrometers, Detectors and Associated Equipment* 975 (2020), p. 164197. ISSN: 0168-9002. DOI: https://doi.org/10.1016/j.nima.2020.164197. URL: https://www.sciencedirect.com/science/article/pii/S0168900220305933 (cit. on p. 3).

[19] A. Knyazev, J. Park, P. Golubev, et al. “Simulations of light collection in long tapered CsI(Tl) scintillators using real crystal surface data and comparisons to measurement”. In: *Nuclear Instruments and Methods in Physics Research Section A: Accelerators, Spectrometers, Detectors and Associated Equipment* 1003 (2021), p. 165302. ISSN: 0168-9002. DOI: https://doi.org/10.1016/j.nima.2021.165302. URL: https://www.sciencedirect.com/science/article/pii/S0168900221002862 (cit. on p. 3).

[20] N. Eno. *Calorimeters for high energy colliders*. https://indico.fnal.gov/event/43762/contributions/192682/attachments/132712/163711/eno_calorimeters.pdf (cit. on p. 3).

[21] M. Aleksa et al. *Calorimeters for the FCC-hh*. 2019. arXiv: 1912.09962 [physics.ins-det] (cit. on p. 3).

[22] W. B. Atwood, A. A. Abdo, M. Ackermann, et al. “THE LARGE AREA TELESCOPE ON THE FERMI GAMMA-RAY SPACE TELESCOPE MISSION”. In: *The Astrophysical Journal* 697.2 (May 2009), p. 1071. DOI: 10.1088/0004-637X/697/2/1071. URL: https://dx.doi.org/10.1088/0004-637X/697/2/1071 (cit. on p. 3).

[23] A. Navrotsky. “New Developments in the Calorimetry of High-Temperature Materials”. In: *Engineering* 5.3 (2019), pp. 366–371. ISSN: 2095-8099. DOI: https://doi.org/10.1016/j.eng.2019.03.003. URL: https://www.sciencedirect.com/science/article/pii/S2095809918307367 (cit. on p. 3).

[24] C. W. Fabjan and F. Gianotti. “Calorimetry for Particle Physics”. In: *CERN-EP/2003-075* (Oct. 2003). URL: https://cds.cern.ch/record/706090/files/cer-003075512.pdf (cit. on p. 3).

[25] I. Alkhatib, D. W. P. Amaral, and et al. Aralis. “Light Dark Matter Search with a High-Resolution Athermal Phonon Detector Operated above Ground”. In: *Physical Review Letters* 127.6 (2021). ISSN: 1079-7114. DOI: 10.1103/physrevlett.127.061801. URL: http://dx.doi.org/10.1103/PhysRevLett.127.061801 (cit. on p. 3).

[26] Nuclear Power. https://www.nuclear-power.com/nuclear-engineering/radiation-detection/scintillation-counter-scintillation-detector/scintillation-materials-types-of-scintillators/. Accessed: April 22, 2024. 2024 (cit. on p. 3).

[27] N. Tsoulfanidis and S. Landsberger. *Measurement detection of radiation, 4th edition*. Jan. 2015, pp. 195–216 (cit. on pp. 4, 9, 11).

[28] R. Novotny. “Inorganic scintillators—a basic material for instrumentation in physics”. In: *Nuclear Instruments and Methods in Physics Research Section A: Accelerators, Spectrometers, Detectors and Associated Equipment* 537.1 (2005). Proceedings of the 7th International Conference on Inorganic Scintillators and their Use in Scientific and Industrial Applications, pp. 1–5. ISSN: 0168-9002. DOI: https://doi.org/10.1016/j.nima.2004.07.221. URL: https://www.sciencedirect.com/science/article/pii/S0168900204017723 (cit. on p. 4).

[29] M. Winkel. “Komplexe Pulsformalgorithmen und Teilchenidentifikation zur Echtzeit-Implementierung in CALIFA”. PhD thesis. Technische Universität München, 2016 (cit. on p. 6).

[30] O. Tengblad, T. Nilsson, Nácher, et al. “LaBr3(Ce):LaCl3(Ce) Phoswich with pulse shape analysis for high energy gamma-ray and proton identification”. In: *Nuclear Instruments and Methods in Physics Research Section A: Accelerators, Spectrometers, Detectors and Associated Equipment* 704 (2013), pp. 19–26. ISSN: 0168-9002. DOI: https://doi.org/10.1016/j.nima.2012.11.094. URL: https://www.sciencedirect.com/science/article/pii/S0168900212014416 (cit. on p. 6).

[31] R3B Collaboration. *Technical Report for the Resign, Construction and Commissioning of the Cracking Detectors for R3B*. Tech. rep. R3B Collaboration, Nov. 2014. URL: https://edms.cern.ch/document/1865815/LAST_RELEASED (cit. on pp. 7, 49).

[32] W. Leo. *Techniques for nuclear and particle physics experiments: A how-to approach*. Springer, 1994 (cit. on p. 9).

[33] R. Evans. *The Atomic Nucleus*. New York: McGraw-Hill, 1955 (cit. on p. 12).

[34] R. Fitzpatrick. https://farside.ph.utexas.edu/teaching/336k/Newton/node51.html. Accessed: March 26, 2024. 2011 (cit. on p. 13).

[35] FischerScientific. https://www.fishersci.com/us/en/periodic-table.html. Accessed: March 26, 2024. 2024 (cit. on p. 14).

[36] R. L. Workman et al. “Review of Particle Physics”. In: *PTEP* 2022 (2022), p. 083C01. DOI: 10.1093/ptep/ptac097 (cit. on p. 15).

[37] H. Bethe. “Zur Theorie des Durchgangs schneller Korpuskularstrahlen durch Materie”. In: *Annalen der Physik* 5 (1930). DOI: https://doi.org/10.1002/andp.19303970303 (cit. on p. 15).

[38] F. Salvat. “Bethe stopping-power formula and its corrections”. In: *Phys. Rev. A* 106 (3 Sept. 2022), p. 032809. DOI: 10.1103/PhysRevA.106.032809. URL: https://link.aps.org/doi/10.1103/PhysRevA.106.032809 (cit. on p. 16).

[39] J. Seguinot and T. Ypsilantis. “Photo-ionization and Cherenkov ring imaging”. In: *Nuclear Instruments and Methods* 142.3 (1977), pp. 377–391. ISSN: 0029-554X. DOI: https://doi.org/10.1016/0029-554X(77)90671-1. URL: https://www.sciencedirect.com/science/article/pii/0029554X77906711 (cit. on p. 17).

[40] M. Adinolfi, G. Rinella, Albrecht, et al. “Performance of the LHCb RICH detector at the LHC”. In: *The European Physical Journal C* 73.5 (May 2013). ISSN: 1434-6052. DOI: 10.1140/epjc/s10052-013-2431-9. URL: http://dx.doi.org/10.1140/epjc/s10052-013-2431-9 (cit. on p. 17).

[41] S. Bheesette. “Design and Characterisation Studies of Resistive Plate Chambers”. PhD thesis. Indian Inst. Tech., Mumbai, 2009 (cit. on p. 19).

[42] C. Lippman. “Detector Physics of Resistive Plate Chambers”. PhD thesis. Naturwissenschaften vorgelegt beim Fachbereich Physik der Johann Wolfgang Goethe-Universität in Frankfurt am Main, 2003 (cit. on pp. 19, 21–23).

[43] CERN. https://home.cern/science/accelerators. Accessed: April 15, 2024. 2024 (cit. on p. 19).

[44] J. Keuffel. “Parallel-Plate Counters”. In: *Review of Scientific Instruments* 20.3 (Mar. 1949), pp. 202–208. ISSN: 0034-6748. DOI: 10.1063/1.1741489. eprint: https://pubs.aip.org/aip/rsi/article-pdf/0/3/202/19030694/202_1_online.pdf. URL: https://doi.org/10.1063/1.1741489 (cit. on p. 19).

[45] P. Galison. *Image and Logic: A Material Culture of Microphysics*. University of Chicago Press, 1997 (cit. on p. 19).

[46] E. Badura, V. Dodokhov, J. Eschke, et al. "Status of the Pestov spark counter development for the ALICE experiment". In: *Nuclear Instruments and Methods in Physics Research Section A: Accelerators, Spectrometers, Detectors and Associated Equipment* 379.3 (1996). Proceedings of the Sixth International Conference on Instrumentation for Experiments at e+ e- Colliders, pp. 468–471. ISSN: 0168-9002. DOI: https://doi.org/10.1016/0168-9002(96)00569-4. URL: https://www.sciencedirect.com/science/article/pii/0168900296005694 (cit. on p. 20).

[47] H. Kumagai, T. Ohnishi, N. Fukuda, et al. "Development of Parallel Plate Avalanche Counter (PPAC) for BigRIPS fragment separator". In: *Nucl. Instrum. Meth. B* 317 (2013). Ed. by Hiroyoshi Sakurai et al., pp. 717–727. DOI: 10.1016/j.nimb.2013.08.050. arXiv: 1311.0215 [physics.ins-det] (cit. on p. 20).

[48] A. Arefiev, G. Bencze, A. Bizzeti, et al. "Parallel plate chambers: a fast detector for ionizing particles". In: *Nuclear Instruments and Methods in Physics Research Section A: Accelerators, Spectrometers, Detectors and Associated Equipment* 348.2 (1994), pp. 318–323. ISSN: 0168-9002. DOI: https://doi.org/10.1016/0168-9002(94)90754-4. URL: https://www.sciencedirect.com/science/article/pii/0168900294907544 (cit. on p. 20).

[49] R. Santonico and R. Cardarelli. "Development of resistive plate counters". In: *Nuclear Instruments and Methods in Physics Research* 187.2 (1981), pp. 377–380. ISSN: 0167-5087. DOI: https://doi.org/10.1016/0029-554X(81)90363-3. URL: https://www.sciencedirect.com/science/article/pii/0029554X81903633 (cit. on p. 20).

[50] R. Ganai, M. Mondal, S. Mehta, et al. "Development and Characterization of 6-gap Bakelite Multigap Resistive Plate Chamber". In: *JINST* 13.07 (2018), P07022. DOI: 10.1088/1748-0221/13/07/P07022. arXiv: 1806.08265 [physics.ins-det] (cit. on p. 21).

[51] E. Zeballos, I. Crotty, Hatzifotiadou, et al. "A New type of resistive plate chamber: The Multigap RPC". In: *Nucl. Instrum. Meth. A* 374 (1996), pp. 132–136. DOI: 10.1016/0168-9002(96)00158-1 (cit. on p. 21).

[52] P. Camarri, R. Cardarelli, A. Ciaccio, et al. "Streamer suppression with SF6 in RPCs operated in avalanche mode". In: *Nuclear Instruments and Methods in Physics Research Section A: Accelerators, Spectrometers, Detectors and Associated Equipment* 414.2 (1998), pp. 317–324. ISSN: 0168-9002. DOI: https://doi.org/10.1016/S0168-9002(98)00576-2. URL: https://www.sciencedirect.com/science/article/pii/S0168900298005762 (cit. on p. 22).

[53] R. Cardarelli, V. Makeev, and R. Santonico. "Avalanche and streamer mode operation of resistive plate chambers". In: *Nuclear Instruments and Methods in Physics Research Section A: Accelerators, Spectrometers, Detectors and Associated Equipment* 382.3 (1996), pp. 470–474. ISSN: 0168-9002. DOI: https://doi.org/10.1016/S0168-9002(96)00811-X. URL: https://www.sciencedirect.com/science/article/pii/S016890029600811X (cit. on p. 22).

[54] ATLAS Collaboration. *ATLAS muon spectrometer: Technical Design Report*. Tech. rep. May 1999. URL: https://cds.cern.ch/record/391176/files/cer-0317330.pdf (cit. on p. 22).

[55] J. G. Layter. *The CMS muon project: Technical Design Report*. Tech. rep. 1997. URL: https://cds.cern.ch/record/343814/files/LHCC-97-032.pdf (cit. on p. 22).

[56] R. Arnaldi et al. “Study of resistive plate chambers for the Alice dimuon spectrometer”. In: *Nucl. Phys. B Proc. Suppl.* 78 (1999). Ed. by E. Borchi et al., pp. 84–89. DOI: 10.1016/S0920-5632(99)00527-7 (cit. on p. 22).

[57] D. Belver, P. Cabanelas, E. Castro, et al. “Performance of the low-jitter high-gain/bandwidth front-end electronics of the HADES tRPC wall”. In: *IEEE Transactions on Nuclear Science* 57.5 PART 3 (2010). Cited by: 29, pp. 2848–2856. DOI: 10.1109/TNS.2010.2056928. URL: https://www.scopus.com/inward/record.uri?eid=2-s2.0-79953792916&doi=10.1109%2fTNS.2010.2056928&partnerID=40&md5=6b784d68c6232769e9f53178d1e5af9d (cit. on p. 24).

[58] D. Bertini. “R3BRoot, simulation and analysis framework for the R3B experiment at FAIR”. In: *Journal of Physics: Conference Series* 331.3 (Dec. 2011), p. 032036. DOI: 10.1088/1742-6596/331/3/032036. URL: https://dx.doi.org/10.1088/1742-6596/331/3/032036 (cit. on p. 25).

[59] D. Bertini, M. A-Turany, I. Koenig, et al. “The FAIR simulation and analysis framework”. In: *Journal of Physics: Conference Series* 119.3 (July 2008), p. 032011. DOI: 10.1088/1742-6596/119/3/032011. URL: https://dx.doi.org/10.1088/1742-6596/119/3/032011 (cit. on p. 25).

[60] Geant4 Collaboration. https://geant4.web.cern.ch/. Accessed: May 23, 2024 (cit. on p. 25).

[61] I. Hrivnacova, D. Adamova, V. Berejnoi, et al. “The Virtual Monte Carlo”. In: (June 2003) (cit. on p. 25).

[62] R. Brun and F. Rademakers. “ROOT: An object oriented data analysis framework”. In: *Nucl. Instrum. Meth. A* 389 (1997). Ed. by M. Werlen and D. Perret-Gallix, pp. 81–86. DOI: 10.1016/S0168-9002(97)00048-X (cit. on p. 27).

[63] R3B Collaboration. *PAS: Proton Arm Spectrometer*. Addendum to the Technical Report for the Design, Construction and Commissioning of the Tracking Detectors for R3B. Technical Report. Institut für Kernphysik, Technische Universität Darmstadt et al., Apr. 2024 (cit. on pp. 52, 53).

Appendix A

Additional Data

Table A.1: This table presents data for protons, deuterons, and alphas across varying energy levels, comparing momentum, reconstructed momentum, sigma, resolution, and peak efficiency in setups with and without CALIFA.

Setup	Particle	Energy (MeV/u)	Momentum (MeV/c)	Reconstructed Momentum (MeV/c)	Sigma (MeV/c)	Resolution	Peak Efficiency
Setup without CALIFA	Protons	400	958	957.9	9.5×10^{-3}	10^{-3}%	94.2%
		500	1094.5	1094.5	8.7×10^{-3}	8.0×10^{-4}%	91.9%
		700	1348.8	1348.7	7.3×10^{-3}	5.0×10^{-4}%	90.6%
	Deuterons	400	1915.6	1921.1	9.3×10^{-3}	5.0×10^{-4}%	92.0%
		500	2188.5	2194.9	8.5×10^{-3}	4.0×10^{-4}%	90.4%
		700	2696.8	2704.7	7.3×10^{-3}	3.0×10^{-4}%	85.0%
	Alphas	400	3806.7	3831.4	2.5×10^{-2}	7.0×10^{-4}	91.3%
		500	4349	4377.4	2.3×10^{-2}	5×10^{-4}%	91.5
		700	5359.2	5394.4	2.3×10^{-2}	4×10^{-4}%	91.7%
Setup with CALIFA	Protons	400	958	785.3	13.30	1.69%	49.9%
		500	1094.5	973.8	8.95	0.92%	49.2%
		700	1348.8	1263.9	6.70	0.53%	48.5%
	Deuterons	400	1915.6	1798.4	8.30	0.46%	49.1%
		500	2188.5	2099.3	7.60	0.36%	47.0%
		700	2696.8	2633.3	9.30	0.35%	50.0%
	Alphas	400	3806.7	3138.1	41.70	1.33%	46.8%
		500	4349	3896.5	32.40	0.83%	50.9%
		700	5359.2	5058.5	25.80	0.51%	47.9%

Table A.2: This table presents data for protons, deuterons, and alphas across varying energy levels, comparing momentum, reconstructed momentum, sigma, resolution, and peak efficiency in setups with CALIFA. Shows results for all the setups considered.

Setup (CALIFA included)	Particle	Energy (MeV)	Momentum (MeV/c)	Reconstructed Momentum (MeV/c)	Sigma (MeV/c)	Resolution	Peak Efficiency
Setup with Block	Protons	400	958	755.9	13.2	1.75%	20.2%
		500	1094.5	964.1	11.4	1.18%	43.2%
		700	1348.8	1261.8	7.4	0.59%	41.0%
	Deuterons	400	1915.6	1793.4	10.1	0.56%	39.6%
		500	2188.5	2095.4	8.7	0.42%	38.8%
		700	2696.8	2631	9.5	0.36%	35.3%
	Alphas	400	3806.7	3029.8	75.2	2.48%	25.6%
		500	4349	3860	40.2	1.04%	47.7%
		700	5359.2	5050	35.7	0.71%	43.0%
Setup with Jitter	Protons	400	958	788.2	20.7	2.63%	53.4%
		500	1094.5	976.4	25.9	2.65%	55.8%
		700	1348.8	1267.6	46.2	3.64%	57.8%
	Deuterons	400	1915.6	1800.9	42.2	2.34%	59.3%
		500	2188.5	2095.6	60.7	2.90%	59.5%
		700	2696.8	2624.7	98.3	3.75%	60.6%
	Alphas	400	3806.7	3145.3	80.5	2.56%	55.5%
		500	4349	3911.6	123.6	3.16%	66.7%
		700	5359.2	5063.4	215.7	4.26%	70.7%
Setup with Block and Jitter	Protons	400	958	755.5	17.6	2.33%	21.7%
		500	1094.5	965.2	29.6	3.07%	50.0%
		700	1348.8	1259.1	51.7	4.11%	53.0%
	Deuterons	400	1915.6	1793.2	46.1	2.57%	50.6%
		500	2188.5	2083.7	67.9	3.26%	55.3%
		700	2696.8	2624	114.6	4.37%	55.2%
	Alphas	400	3806.7	3050.3	101.4	3.32%	29.7%
		500	4349	3857.1	161.9	4.20%	69.1%
		700	5359.2	4982.3	249.3	5.00%	72.9%